MACQUARIE UNIVERSITY

The recognition of quartz grown from a melt

during static and dynamic conditions

Joyjit Dey

Masters of Research Thesis
Department of Earth and Planetary Sciences

Submission date: 10/10/2018
Duration of thesis work- Jan, 2018 to Oct, 2018 (~ 10 months)

Department of Earth & Planetary Sciences in

The Faculty of Science and Engineering,
Macquarie University, North Ryde,
Australia

MACQUARIE
University
SYDNEY·AUSTRALIA

Cover photo courtesy of N. Daczko

Statement of originality:

I, Joyjit Dey, declare that, to the best of my knowledge, the work presented herein is the original work of the author and has not been presented or published elsewhere. All published works and work carried out by persons other than me presented here are appropriately referenced and due respect given to the participants. Further no part of this work has been presented, accepted or been published for the award or consideration of a higher degree at this or any other educational institution.

Signed:

Joyjit Dey

11/10/2018

Acknowledgements

This past nine month was a roller coaster ride for me, moving out from a nest to a whole new world of academia is scary, but outright exciting at the same time. The places I've been fortunate enough to travel have given me immense experience and fun to grow as a human being. However, it takes more than just one person to complete a project of this scale and as such, there are several people I would like to thank.

I would first like to thank my thesis advisor Prof. Nathan Daczko. The door to Nathan was always open whenever I ran into a trouble spot or had a question about my research or writing. And, then to Prof. Sandra Paizolo at the University of Leeds, without her faith and support, it would have never been possible for me to quit my earlier job and start off this exciting journey through academia. She always provided me support during my days of apathy. I admire both of your incredible knowledge in metamorphic and structural geology, your big picture visualization and most of all, your passion. Sandra for her incredible magnanimity in supporting my trip over to Leeds to work with her at the University. The constant assistance and your expert knowledge and passion for science, your quick revisions, and Skype meetings were very much appreciated. It has been an immense pleasure working with both of you and I wish the best for you and your families.

I thank Dr. John Wheeler of Liverpool University, who not only let me use his codes of 'Crystal Scape' software but also provided me with adequate information when I got stuck. Dr. Kim Jessop and Dr. Cait Stuart for your extreme generosity to lend me use your rock samples, and then Kim your comprehensive knowledge about the WMC provided us through support during the field trip. Thanks to Dr. Luke Milan of New England University for chauffeuring through the field, and to his wife Leana for providing us food, hot beverages, and shelters – the most luxurious fieldwork I've ever done. Thank you. Robyn Gardner for the information you retained and being able to feed me in whenever needed. Mucking around with various codes in the MTEX to be able to get our way through was an exciting learning period. To the buddy Hindol Ghatak, for providing me the safe haven, warm food and whatnot from the very first day in Sydney.

Duncan Hedges (Leeds), and Tim Murphy (MQ) for the first-hand information on EBSD and helping me out to get on with all my EBSD analyses from time to time. Steve and Manal, and John (Leeds) for putting up with the slow trickle of thin sections through this whole period. I thank Alex Stokes for letting me access the Optofab node of the Australian National Fabrication facility at MQ.

To the several academic staff from the EPS department who have provided assistance at various stages of this project. The warmth and support received from the friends and colleagues at the department are worth mentioning. A special mention for Zairong, Thusitha, Marina, Sinan, and Alex.

Lastly, but definitely not least, my parents and aunt for their love, support, and belief. Thanks a lot, Aditi, for being there for the last four years and tolerating an annoyingly reclusive person like me.

<u>TABLE OF CONTENTS</u>

Abstract:

Quartz microstructures are routinely used to establish the nature of solid-state deformation mechanisms. However, it is unclear which microstructures are typically developed in a melt present environment compared to a solid state, and how to distinguish between these two. The microstructural features of quartz crystallizing from a silicate melt are investigated in a) slowly cooled granite, b-c) statically heated and cooled, and actively deforming migmatites, and d) in a melt-fluxed high strain zone. This study takes a holistic approach integrating microscopic observation along with electron back scatter diffraction (EBSD) and weighted burgers vector (WBV) analysis. Results show quartz pseudomorphing melt pockets forms sub-grain boundaries and shows crystal bending, and change in orientation very similar to a solid-state deformation. EBSD and WBV analyses identify dislocations on both basal plane and non-basal plane, and identify <a> slip and [c] slip, and sometimes a combination of both. Existence of slip-systems, though without a crystallographic preferred orientation (CPO), suggests the features are dependent on local stresses rather than regional differential stress, and are interpreted to be a result of mineral growth in pore spaces when the melt crystallizes. Differences to solid state deformation microstructures include well connected grains in 3D, lack of CPO, lack of grain shape preferred orientation, and high dauphine twin frequency at grain boundaries.

Chapter 1: Introduction

A strong feedback between melt migration and deformation has already been established based on field observations and microstructural study for both crustal and mantle shear zone (Tomassi et al., 1994; Kelemen and Dick, 1995; Rosenberg, 2004 etc.). All these models discuss syntectonic melt (or aqueous fluid) percolation and localization of strain in the rock mass, but no studies have focused to date explicitly on the internal-microstructure and evolution of microstructure with time of minerals crystallising from interstitial fluid phase with or without active regional stress. Also, the composition of upper crust is dominated by quartzo-feldspathic rocks, largely represented by granitoid plutons, metagranitoids, orthogneisses and felsic volcanics which are products of melting of the lower to middle crust (Rapp et al., 1991; Wolf and Wylie, 1994; Brown 2010). Thus partial melting, melt migration and emplacement of plutons are elemental processes responsible for the differentiation of the continental crust (Taylor and McLennan, 1995; Brown and Rushmer, 2006). Transfer of melts from depth includes dykes, high strain zones and porous melt flow. Even though it has been shown that mid-crustal ductile shear zones may be highly permeable fluid conduits (e.g. Menegon et al., 2015), little attention has been placed on the fact that both aqueous fluid and silicate melts may migrate through such conduits. Until recently, little detailed work has been performed focussing on recognizing the transgressing fluids as silicate melts (Stuart et al., 2016, 2017). In contrast, analysis into the mode of solid state deformation, is now standard. With the advent of quantitative orientation analysis (e.g. EBSD) much of this work has concentrated in establishing microstructural signatures (e.g. Halfpenny et al., 2006; Dempsey et al., 2011; Okudaira and Shigematsu, 2012 etc.), but for the analysis of rock with some melt presence, such studies are still relatively uncommon, and generally only concentrate on bulk crystallographic orientation. Many features used to describe solid-state deformation such as misorientation axes, boundary distributions and internal deformation characteristics have not been analysed in rocks where melt was present. Hence, despite its importance, at present, the characteristics that can be used to distinguish quartz grown from melt or aqueous fluid with or without accompanying deformation have not been established.

This contribution aims to close this gap in our knowledge by linking the microstructural features identified under the microscope to quantitative orientation analysis. On the basis of the results, it is possible to identify the processes that occur during crystallization in a melt

versus aqueous fluid and link these to associated microstructural features. In this systematic study, rocks of differing, known geological history are investigated.

I) Microstructures of melt-bearing rocks

a) Microstructures typical for slow crystallization in igneous Granite and Granodiorite rocks: a static case

Granitoid plutons are thought have undergone slow crystallization as they are constructed into large rock masses by a) pulsed magma addition over protracted geological time resulting in a relatively lengthy cooling history (Coleman et al., 2004; Clemens et al., 2017a, b) or b) grain mushes accumulated as residue left behind after removal of fractionated liquids (Bachmann and Bergantz 2004; Glazner et al., 2004; Keller et al., 2015). There is still some debate if microstructures now observed within granites originate from crystallization during initial magma cooling or from subsolidus recrystallization and solid-state grain growth obliterating much of the magmatic features (Hibbard, 1965; Pitcher, 1979; Coleman et al., 2005 etc.). However, there are several features conclusive of limited microstructural change after initial cooling as summarised in Table. 1 (Vernon and Paterson, 2008).

During solidification, the initial static grain growth is controlled by the kinetics of the solid-liquid interfaces, whereas the grain size variation depends on the balance between growth and grain-nucleation. The grain boundaries are morphologically characteristic of the environment in which grains are growing, and are typically irregular (Holness et al., 2007) (Tab. 1). However, magmatic flow can lead to the development of planer grain boundaries (i.e boundaries parallel to growth faces) (Vance, 1969; Graeter et al., 2015; Vukmanovic et al., 2018). The microstructure of non-deforming igneous rocks fall on a spectrum of two end members (Holness et al., 2018) (Tab. 1). In the first category, the microstructure is controlled entirely by the kinetics of crystal growth; thus is required to be in a relatively rapidly cooled environment (but enough to grow large euhedral crystals), and give rise to rough interfaces (Tab. 1). In the other category, the microstructure is directed by the minimisation of internal energies (in order to attain textural equilibrium) by diffusive mass transport for rocks that remained at higher temperatures for a significant time period and textural equilibrium keeps pace with the crystal growth. A long period of undercooling (reduced undercooling) would facilitate formation of planer interfaces joined by smooth rounded edges (Herring, 1951; Holness et al., 2108). Hypersolidus textural equilibrium approaches the lowest energy configuration and ensures equilibration of a melt-solid-solid low dihedral angle at all three grain junctions (Tab. 1). An angle of less than 60° would imply complete connectivity of

pores (Holness, 2006). In comparison, in high grade texturally equilibrated metamorphic rocks, subsolidus solid-solid-solid dihedral angle approaches 120°. Deformation is cited as one of the most important process that could overprint original magmatic microstructure by dislocation creep, dissolution-reprecipitation, and melt enhanced grain boundary sliding (Paterson, 1995, 2001). However, significant changes in grain shape and size, or the creation of a crystallographic preferred orientation during deformation would be anticipated in such conditions (Holness, 2018) (Tab. 2). An onset of melt-present brittle deformation followed by a high temperature crystal-plastic deformation can also be observed at a pluton margin as a result of the expansion of a plutonic body by intrusion of magmas in the interior (Ramsay, 1989; Clemens, 1998; Paterson et al., 1989; Vernon et al., 2004). Though, a minor strain accumulation (as subgrains in quartz/ minor grain boundary migration in feldspar) in an otherwise undeformed granite is mentioned in Vernon and Paterson, 2008, but no work has still been carried out on characterization of those minor solid state adjustments.

b) Microstructures typically found in migmatites in contact aureoles' (static) and regionally metamorphosed molten rocks (dynamic migmatite):

Migmatites are hybrid heterogeneous rocks, with properties pertaining to both igneous and metamorphic rocks, formed during anatexis at high P-T metamorphic conditions and having light banding (leucosomes) and dark layers (melanosomes and paleosomes). While the leucosome is mineralogically simple with quartz and feldspar, the paleosome/melanosome is usually associated with remnant high-grade mafic metamorphic minerals of high-temperature grade (Tab. 1). During migmatisation, the reactant phases become unstable and give rise to melting at triple junctions between them. Whether the melt moves out of the system or not depends on the driving force to squeeze it out, and a dilatant site for it to collect (Sawyer, 1999). In the case of a hydrostatic stress, if the melt fraction remains below 15%, it does not leave the solid matrix and the system behaves as a closed system. In the following this case is referred to as the *static case* (Tab. 1). In contrast, when a deviatoric stress is applied on the system the melt tends to push out and the system may appear to be open at the sample or outcrop scale. In the following this case is referred to as the *dynamic case* (Sawyer, 1999) (Tab. 1). Retrograde replacement textures are very common in both of these migmatitic rock types forming a typical low-grade assemblage (Ashworth, 1972, 1979). Post-crystallization and cooling, migmatites tend not to deform in a solid-state (e.g. Prakash et al. 2018, Lee et al. 2018).

Though it is straightforward to deduce the former presence of melt when there is outcrop-scale segregated leucosome layers and/or injected melt veins/networks in migmatites, or even a high-temperature mineral assemblage, it is much more difficult when the melt has been largely extracted. Also, magmatic microstructure can get modified (or even obliterated) by post-melting deformation and recrystallization-neocrystallization overprinting the high temperature event (Vernon, 2011).

When the melt is of sufficiently low viscousity compared to the surrounding solid rock, it can flow and make a 'continuous flow-channel network' along the grain edges forming low dihedral angles (LDA) of ≤60° (Smith, 1957) (Tab. 1). However, when melt crystallizes slowly as found in regional metamorphic terrains (in migmatites) these angles tend to approach low energy solid-solid boundary angles (Holness, 2008), and therefore they are only a reliable indicator if surrounding embayed melted grains of the original rock can be identified (Tab. 1). However, melt pseudomorphs having a low dihedral angle were also observed in regional metamorphic rock (Guernina and Sawyer, 2003; Hasalová et al., 2008a etc.). Thus, a close inspection must be followed while using low dihedral angles as main criteria of the former presence of melt. Depending on the relative proportion of the quartz to feldspar in the solid framework of a partially melted rock, the crystallizing felsic melt decides which one of the phases will be 'interserts' i.e bounded by one or the more grains with euhedral faces (terminology used by Cmíral et al., 1998). In the absence of deformation (i.e. 'static case') and if the temperature is permitted to change very slowly, the textural equilibrium will be attained very easily. Thus, in static migmatites, a silicate melt is found to be interconnected by a stable network of channels along three-grain junctions, even if only a few percent of melt is present (Tab. 1). This process is called- diffusive porous flow (Scott and Stevenson, 1986; Turcotte and Ahern, 1978). Cuspate shaped minerals of quartz, K-feldspar or plagioclase with sharp pointed extensions form due to the low dihedral angle (Holness and Clemens, 1999; Clemens and Holness 2000; Sawyer, 2001) (Tab. 1). Sometimes simultaneous crystallized aggregates of quartz-plagioclase-Kfs can also be seen and are more common in contact aureoles (Tab. 1). In regional metamorphic migmatites euhedral inclusion-free overgrowths of peritectic minerals on inclusion-rich residual grains infer grain growth in a fluid (here a melt) rich environment (Tab. 1). Also, magmatic flow can occur in diffuse zones of migmatites leading to aligned, euhedral, undeformed plagioclase crystals (Sawyer, 2001; Vernon, 2011). The presence of patches of peritectic minerals (melanosomes) indicates sites of former partial melting from which melts have largely been extracted (Sawyer et al., 1999; White et al., 2004) (Tab. 1). The 'back reaction'

between peritectic minerals and cooling melt producing 'symplectic replacement' aggregates and coronas are consistent with the former presence of melt (Ashworth, 1976; Sawyer, 1999; Jones and Brown, 1990; Vernon, 2011 etc.).

c) Microstructures typical of a melt present shear zone: a dynamic case

Leucosome filled shear bands and shear zones containing crystallized previous melt in migmatitic terranes are often cited as evidence of coeval melting and shearing (e.g. Weinberg et al., 2009, 2015; Brown and Solar, 1999). Melt bearing rock behaves in a ductile manner and the effect of deformation on the developing microstructure is governed by the rate of deformation versus the energy drive to achieve textural equilibrium (Marchildon and Brown, 2002). Depending on the deforming stress magnitude and the fraction of melt present in a rock, the grain-scale melt distribution can localize along the foliation plane or could form elongate pockets aligned at a high angle to the foliation plane (Tab. 1) (Roseneberg and Riller, 2000; Sawyer, 2001; Marchildon and Brown, 2002; Zàvada et al., 2007). The melt gets sucked into the grain boundaries that open during shearing (along the foliation plane) when the stress is fairly low and melt volume is only <2%. Whereas at higher stress and higher melt percentages, the grain boundaries sitting at an angle to foliation begin to dilate (Schulmann et al., 2008). At higher degrees, a switch in deformation mechanism from melt fraction dependent dislocation creep to diffusion accommodated grain boundary sliding takes place. A pronounce effect on rock microstructure can be seen at a Melt Connectivity Threshold (MCT) for a melt fraction as low as ~0.07 (Rosenberg and Handy, 2005). Melt flow in a partially molten rock at high pressure occurs when its fraction transiently reaches the rheological critical limit percentage (RCMP) even if transiently in the core of a viscoelastic anatectic rock (Zavada et al.,2018).

The matrix grains from which melt has been squeezed out undergo dynamic grain boundary migration recrystallization. Also dynamically crystallized melt (i.e under deviatoric stress) sometimes enhances the wetting of grain boundaries and shows intergranular and, occasionally, intragranular fracture (Tab. 1) (Roseneberg and Riller, 2000). When felsic melt crystallizes in the smallest pores, it forms melt pseudomorphs (formed by any of their cotectic composition) and if it crystallizes in larger melt pockets, it tends to develop polymineralic aggregates (Tab. 1) (Holness and Swayer, 2008). Melt films can be observed along grain edges or in cracks (Tab. 1), and is pseudomorphed either by quartz, K-feldspar or sodic feldspar (Mehnert et al., 1973; Laporte, 1994; Vernon, 2011). Veinlets of plagioclase, with more sodic composition or having oscillatory zoning, proves

crystallization in felsic melt (Vernon, 2011; Rosenberg and Riller, 2000; Haslová et al., 2008a). Partial melting of biotite and/or it being pseudomorphed by feldspar are indicative of melt reaction in a rock and is a good criteria for former presence of melt (Sawyer, 2001; Vernon, 2011). Microgranophyric intergrowth of quartz and alkali feldspar in the veinlets, found in mid to shallow crustal rocks, is thought to represent pseudomorphed cooling felsic melt (Tab. 1) (Holness and Swayer, 2008; Vernon, 2011).

Previous studies on melt present shear zones have seen a transition from augen gneiss (or banded gneisses) to granofels as the deformation intensity increases. Increased deformation obliterates older fabrics/layering and precipitates newer grains at interstices from percolating fluid and/or melt in the core of the shear zone (Lonka et al., 1998; Hasalová et al., 2008a, 2008b; Zavada et al., 2018). This transition marks a change of deformation mechanism by dislocation creep coupled with melt induced grain boundary sliding (in orthogneisses/mylonite) to a melt enhanced granular glow in granofels with increasing dilation of more grain boundaries at higher strain rate (Zavada et al., 2007, 2018; Schulmann et al., 2008b). But the mechanism of active deformation assisted porous granular melt flow at higher strain and its recognition in the field is still ambiguous. The corresponding microstructure gives rise to diffuse boundaries of granofels and a strong CPO fabric due to the oriented interstitial grain growth, different to a crystal-melt mush of a diatexite (Zavada et al., 2018) (Tab. 1).

II) Quartz microstructures of rocks developed at subsolidus conditions

Many rocks undergo changes at subsolidus conditions by differential stress and/or changes in PT conditions, and most commonly in the presence of an aqueous fluid. Deformation induced solid-state flow has been described extensively (e.g. Hobbs 1968; Vernon 1976, 2000; Paterson et al., 1989). Besides recovery, thermally activated exchange of atoms across the grain boundary of a crystal can lead to the reduction of dislocation density and results in growth of a less deformed crystal at the expense of its more deformed neighbour (Poirier, 1985; Jessell, 1987; Drury and Urai, 1990). This leads to a change in grain size, shape and orientation within the same mineral (Poirier and Guillope, 1979), and the process is known as 'Recrystallization' (Tab. 2). Two fundamental processes that operate during recrystallization are 'Sub Grain Rotation (SGR)' (Poirier and Nicolas, 1975; Guillope and Poirier, 1979) and 'Grain Boundary Migration (GBM)' (Poirier and Guillope, 1979; Poirier, 1985; Drury and Humphreys, 1986).

Ductile deformation by dislocation creep produces a. characteristic preferred orientations of mineral crystallographic axes (CPO) in an otherwise randomly oriented polycrystalline aggregate depending on the slip systems and on the geometry and magnitude of the externally applied stress, and b. formation of sub-planer deformational lamellae (Tab. 2). Deformation of a quartzo-feldspathic rock at the brittle-ductile transition commonly give rise to a mylonite, in which quartz and mica deform in a ductile manner and feldspars show brittle deformation (Debat et al., 1978; Tullis 1979). Important features of simple shear mylonites are based on asymmetry of various fabric elements and structures (Tab. 2). Mylonite under greenschist facies conditions exhibit a. substantial reduction in grain size. b. quartz crystals with intense undulose extinction, recrystallised grain fractions, grain size reduction and long ribbons, c. shear band cleavages, which are commonly known as S-C texture (Gapais and White, 1982), d. mantled porphyroclasts with wide tails and nearly straight outer boundary of the clast or with narrow tails, bends in tails near clast and embayment of matrix (Passchier and Simpson, 1986), e. single mica crystals with their long axis oriented in the direction of extension and showing a small angle with mylonitic foliation- mica fish (Lister and Snoke, 1984), and f. shear extension dragged small folds, also known as a- quarter structure (Tab. 2).

Quartz is probably the single most studied mineral with regard to slip system activation and CPO development (e.g. Hobbs, 1968; Tullis, 1977; Stipp et al., 2002; Vernooji et al., 2006; Menegon et al., 2008; Stipp and Kunze, 2008). During ductile deformation quartz CPO is controlled by temperature, strain rate, differential stress and fluid content. Subgrain boundaries may survive continuous annealing, and later deformation with little modification, and hence are important in deciphering quartz microstructure pertaining to various tectonometamorphic histories (Kruhl, 1996; Law, 2014; Parsons et al., 2016a).

However, metamorphism or solid-state reaction is not always accompanied by deformation. In a contact metamorphic aureole, intrusions liberate heat into the country rock by conducting/advecting percolating fluids and heat the rock under hydrostatic conditions (Turner and Gustafson 1981). In a more open system, the percolating fluid can establish a compositional gradient with the country rock, thus producing metasomatic aureoles (Einaudi, 1977; Rubie and Gunter, 1983; Putnis and Austrheim, 2010 etc.).

Table. 1 *Summary of microstructures of different melt bearing rocks with (dynamic) and without (static) regional differential stress. For references refer to text.*

STATIC	DYNAMIC
A. *Slow crystallization in igneous rock*: **Microstructural features:** • Impingement of two grains having straight or irregular grain boundaries *(during solidification)* • Grain boundaries oriented at high angles to the growth faces sometimes with small inclusions *(during grain growth)* • Elongate crystals of plagioclase with euhedral growth and primary zoning *(crystallized phenocrysts/megacrysts)* • Retention of delicate oscillatory zoning in quartz and plagioclase *(less dynamic recrystallization)* • Euhedral inclusions of plagioclase in K-feldspar, plagioclase in quartz, plagioclase in biotite etc. *(as crystallized from melt)* • Geometry of three grain junction formed by two phases - a) in a *rapidly cooled granite* show wide range of angles forming planer grain boundaries by growth faces b) in a *slowly cooled granite*, a narrow range of angles, with smooth curved grain boundaries • Low dihedral angle (LDA) close to 60°, associated with cuspate grains and thin film of secondary phase along grain boundary *(minimisation of interfacial energy)* • Other primary magmatic features: growth twins in K-Feldspars, plagioclase & hornblende; fine grained intergrowth of minerals having granophyric microstructures **EBSD studies:** • No detailed EBSD work has been performed on an 'undeformed' granite from a plutonic interior or from plutonic boundary *B. Static Migmatite:* **Microstructural features:** • In rapidly cooled contact aureole the melt can freeze as glass *(melt crystallized relatively fast)* • Cuspate shaped minerals of quartz, K-feldspar or plagioclase having sharply pointed extension, and well-developed facets *(grain growth in felsic melt pool)*	A. Regional dynamic migmatite: **Microstructural features:** • Euhedral crystal of feldspar or peritectic minerals (e.g garnet, cordierite, orthopyroxene, Kfs etc.) surrounding protoleucosome *(crystallized phenocrysts/ megacrysts)* • Cuspate volumes of quartz, K-feldspar or sodic plagioclase lining corroded reactant residual grains *(minimisation of interfacial energy)* • Felsic melt veinlets or intragranular fractures, pseudomorphed by either quartz/K-feldspar/plagioclase, and less commonly involving two or three minerals *(crystallized phases from melt)* • Inclusion free *overgrowth* of Kfs or peritectic minerals and *residual* grains with abundant inclusions in the mesosome • Low dihedral angle (LDA) of one mineral against two grains of other mineral at three grain junction *(minimisation of interfacial energy)* • Other features: Plagioclase with oscillatory zoning, veinlets of plagioclase more sodic than plagioclase in the protolith, symplectic replacement aggregates, lobes of myrmekite, and microgranophyric intergrowth in patches, biotites pseudomorphed by feldspar **EBSD studies:** • EBSD studies were carried out by Menegon et al., 2011; Farmer et al., 2017 (Thesis); Prakash et al., 2018 *B. Melt Fluxed Shear Zone:* **Microstructural features:** • Dominantly unimodal grain size distribution *(change from gneiss to granofels with more granular flow of melt)* • Melt pockets parallel or high angle to the foliation, shear bands *(brittle deformation)* • Euhedral/faceted grains crystallized in small interstices and intergrowth of mineral phases in large pores *(pseudomorph melt pockets)*

• Simultaneous crystallization of quartz-Kfs-plagioclase *(grain growth in small interstices)*	• Interstitial quartz (or feldspar) surrounded by feldspar (or quartz). And quartz/feldspar fingers intruding into other grains *(melt pseudomorphs)*
• Reactant minerals with somewhat rounded grain boundaries *(due to melting)*	• Cuspate shaped inclusion of one mineral inside of an another mineral
• Develop more felsic patches than regional migmatites *(due to less deviatoric stress)*	• Xenomorphic grains connected in 3D along grain boundaries and at triple junctions *(minimisation of interfacial energy)*
• Neosome - Paleosome can be identified with its mineralogy	
• LDA developed against two grains of other mineral *(minimisation of interfacial energy)*	• Pseudomorphed melt films *(extremely elongated single grain)*
• Relative proportion of cuspate grains and more compact equant grains show the fraction of melting	• Grains showing low LDA at triple junction against two grains of different mineral phases *(minimisation of interfacial energy)*
EBSD studies:	**EBSD studies:**
• No such EBSD microstructural studies has taken place	• EBSD study discussing CPO only carried out by Stuart et al., 2018

Table. 2 *Microstructures of rocks developed at subsolidus condition*

STATIC	DYNAMIC
A. Hornfels:	*A. Mylonites:*
Microstructural features:	**Microstructural features:**
• Compact and highly metamorphosed contact rock *(solid state reaction under diff. P-T condition)*	• Bimodal grain size distribution *(recrystallization)*
• Granular interlocking grains with variable shapes and sizes *(no tectonic stress)*	• Matrix of small dynamically recrystallized grains *(nucleation of new grains)*
• Composed of silicate and oxide minerals in varying properties	• Elongate porphyroclasts with undulose extinction, subgrains, deformation lamellae and twins *(high strain)*
• Abundant small biotite grains, formed by easy nucleation at numerous rate *(rapid heating cause overstepping of this reaction)*	• High irregular grain boundary *(strain induced grain boundary migration)*
	• Window and pinning structures
	• Shape preferred orientation or lattice preferred orientation *(tectonic stress)*
	• Core-mantle structure *(recrystallization)*
	• Micro-folding, shear bands, and assymmetric microstructure *(tectonic stress)*
	• Brittle and ductile deformation *(stress induced)*
	EBSD studies:
EBSD studies:	• Several EBSD studies have been performed on low-high temperature mylonite, protomylonite orthogneisses, phyllonites examples by Halfpenny et al., 2006; Dempsey et al., 2011; Okudaira and Shigematsu, 2012; Spruzeniece and Piazolo, 2015; Faizo et al., 2017 etc.
• No such EBSD microstructural studies has taken place	

Chapter 2: Methods

a) Fieldwork and Sample selection:

Samples are selected on the basis of their known varied geological history in terms of rate of crystallization and presence or absence of differential stress during crystallization (cf. Tab. 3). Two samples i.e W0809A, WJ1650A from the HTLP Wongwibinda Metamorphic Complex (see below for more details) are chosen as in this area there are well exposed migmatites and post-kinematic granites. Samples are provided by Dr. Kim Jessop, Macquarie University, and were collected as a part of her Ph.D (year 2013-17). To get a better understanding of the field relationships of these samples, fieldwork was conducted between 11-13th February 2018 on the Karuah, Aberfoyle and Lynoch Stations, 50-60 km northeast to Armidale. The area surveyed is a part of the HTLP Wongwibinda Metamorphic Complex and thus provides an excellent set of high temperature molten rocks in the form of exposures bearing migmatite, monzogranite, granodiorite etc. The static migmatite (ST1108B) of Mt. Stafford is provided by Dr. Nathan Daczko, Macquarie University. Samples of melt fluxed shear zone PV1208-2, PV1420H, PV1430H from Fiordland, New Zealand are provided by Dr. Cait Stuart, Macquarie University. The AQ-4 sample shows quartz crystallized from an aqueous fluid and is provided by Dr. Nathan Daczko from the Macquarie University (MQ) teaching collection.

b) Sample preparation:

Samples are cut parallel to the lineation and perpendicular to foliation to obtain desired XZ sections for further EBSD analysis. They were mounted to glass slides and polished to ~30 microns thick.

c) Initial sample characterization:

Polished thin sections are observed under the plane and cross-polarized light using optical microscopy at Macquarie University, Sydney, Australia and the University of Leeds, UK. Back-scatter electron (BSE) imaging is performed on a Hitachi Desktop Scanning Electron microscope (SEM) in the OptoFab node of the Australian National Fabrication Facility, Macquarie University. The operating conditions of the SEM are a low vacuum and 15kv accelerating voltage. Whitney and Evans (2010) is followed for the mineral abbreviations.

d) Quantitative orientation analysis.

Electron Back Scatter Diffraction Analysis (EBSD) and energy dispersive spectroscopy (EDS) data are obtained using the FEI Quanta 650 FEG-ESEM (with Oxford X-max 80 SDD EDS, Oxford/HKL Nordleys EBSD system and Aztec software) at the

Electron Optics Facility, University of Leeds, UK and also at Macquarie GeoAnalytical (Macquarie University, Sydney). Samples are coated with ~3nm of carbon. Analyses are performed with a working distance of ~12mm, an acceleration voltage of 20kV and at a specimen tilt of 70°. 11 EBSD maps were taken across 5 representative samples with step sizes ranging from 0.25-15µm (step size determined by grain size and required resolution). Biotite grains are not indexed as the study mainly focuses on quartz and feldspar microstructures. Only the quartz grains are analysed for the microstructural study. The feldspars are shown only for CPO, and the phases are marked with specific colours.

Maps with higher step size are used to determine the bulk crystallographic preferred orientation (CPO). Here one analysis per grain is performed to nullify the possibility of influence of a single grain over the others. Data are processed in the Oxford Instruments Channel 5 software. Noise reduction and removal of zero solutions are performed following the procedure of Prior et al., 2002; Bestmann & Prior, 2003; Piazolo et al. 2006. Several analyses are performed a. orientation maps of quartz are constructed with IPF_Z1 (inverse pole figure) or Euler colouring. The grain area for a particular grain (measured randomly) and the composition of surrounding phases are observed, b. crystallographic preferred orientation (CPO) of quartz and feldspars; these data are showed as upper hemisphere equal-area projections with 'rainbow contouring'. However, individual grains, which are isolated from each other but placed in the vicinity, may have similar orientation, hence in the pole figure some orientations may show high density, c. characteristic internal change in crystal orientation with respect to a standard mean orientation/ w.r.t a point inside that crystal/ along a profile, are observed, and displayed as 'Local misorientation', 'Textural component', and 'Misorientation profile (MO profile)' respectively. For a 'Textural component map', a maximum 3° change in orientation (w.r.t a fixed point) between two pixels is analysed and then colour coded with rainbow colouring. The maximum misorientation for a single grain is divided by the whole grain area to measure misorientation/area, d. low angle boundaries (subgrain boundaries) with~ 2° (yellow) and 5° (blue) are superposed on top of the pattern quality (band contrast) maps, e. the dauphine twins of quartz are plotted employing the standard dauphine twin law (rotation of 60° w.r.t 'c' axis) and are marked using a red colour. For a single grain, the area surrounded by dauphine boundaries are also measured and then divided by the whole area of that particular grain to quantify dauphine density, f. the single grain pole figures are plotted as upper hemisphere stereographic projections, and the maximum angular dispersion of a single axis is measured using 'Mambo'.

e) Weighted Burgers vector (WBV) analysis:

The dislocations can be calculated as vector field-projected orientation gradients and are called the 'Weighted Burgers Vector (WBV)' (Wheeler et al., 2009; Piazolo et al., 2015). They are the sum over all types of dislocations and measure the intersection densities of dislocation lines with a map. The WBVs are 3D but can be projected on map view as arrows when expressed in sample coordinates. To characterise subgrain walls in terms of vector field, dislocation type, and to quantify dislocation densities here the WBVs are calculated. Here, different domains are marked and local misorientation along with burgers vectors parallel to a1, a2, a3 and c-axis are measured and expressed as K_{a1}, K_{a2}, K_{a3} and K_c. Although the magnitude of WBVs could be influenced by the size of the local region, the direction is not sensitive to this. Here, the presented analysis is restricted to WBVs of length > 0.002 μm^{-1} (Wheeler et al., 2009) to avoid error propagation. The directions are plotted on an IPF, and pole figure using proper filtering. Linear features with high dislocation densities (or long WBVs) characterise subgrain walls. A similar step size of analyses ensures comparability between different samples.

f) Determining slip system activation from EBSD analysis:

Dislocations in distinct subgrain boundaries will form dislocation arrays with a particular rotational axis and small circle dispersions of orientation on pole figures. It is possible to measure orientation of sub-grain boundary along with orientation of misorientation axis in order to define activated slip systems, type of boundary (tilt/twist) and type of dislocations involved (Prior et al., 2002; Piazolo et al., 2008; Menegon et al., 2011; Howell et al., 2012 etc.). Hence, to decipher internal deformation/plastic strain of a crystal lattice small-circle dispersion pattern in pole figures along with misorientation axis distribution are looked into. They are shown for different domains with poles of basal plane, prism planes, and pyramidal planes. Also, <2-1-10> <-12-10> as a1, a2 axis are plotted for quartz. A schematic diagram is drawn following Piazolo et al., 2008 for a subgrain boundary trace for the same data set. The misorientation/ rotational axis is shown by "R.A.". Bold lines are marked and extended outwards from the primitive circle to show the subgrain boundary trace orientation. Two great circles are shown (with blue and green colours) for the reconstructed boundary plane orientation, following a tilt and twist wall model. The plane that contains both the R.A and the subgrain boundary trace forms the likely subgrain boundary plane. Slip plane and slip directions are determined using all the information.

Chapter 3: Sample location and description

a. Static granitoid (monzogranite) and dynamic (syntectonic) migmatite:

Two samples are collected from the Wongwibinda Metamorphic Complex (WMC) in the southern New England Fold Belt (Fig.1). Samples W0809A represents a slowly cooled monzogranite (Tab. 3) and WJ1650A is a metatexite-migmatite. The Wongwibinda Metamorphic Complex, is located in the Nambucca block and is formed by an accreted package of Devonian and Carboniferous deep marine sediments metamorphosed under low pressure (~3.5 kbar) and high temperature conditions (Craven et al., 2012). The most notable feature of this complex is a rapid progression over a short varied distances from fine low grade schists to high grade schists, with migmatites and syn-tectonic S-type granitoids from west to east (Craven et al., 2012). Migmatites are syntectonic. The WMC includes plutonic rocks of the late Carboniferous-early Permian S-type Hillgrove Plutonic suite: The Abroi Granodiorite in the east, the Rockvale adamellite in the south and Tobermory adamellites (now the adamellies are called as monzogranite) in the north (Binns, 1966). Sample W0809A stems from the Rockvale monzogranite, and is collected from near to the pluton margin (Fig. 1, Tab. 3). W0809A represents a sample that cooled slowly under hydrostatic conditions (Tab. 3). Sample WJ1650A stems from the Karuah station and represents a syntectonic migmatite. It is characterized by centimetre scale leucosome bands. Due to its low degree of observed melt content it is classified as a metatexite (Brown, 1973; Sawyer, 2008). The sample represents syntectonic migmatite (Tab. 3).

b. Statically heated and cooled migmatite:

A sample from the regional contact aureole from Mt.Stafford (at a confing pressure of 2.8-4kbar) was chosen to represent an in-situ melted and statically crystallized migmatite (Tab. 3). Mt. Stafford is located in the northwestern end of the Anmatjira-Reynolds Range in the Arunta Block of central Australia (Fig. 1). Within the contact aureole, a well-preserved turbidite sequence was metamorphosed from greenschist to granulite facies (Wang et al., 2014). The aureole experienced minimal strain and retains a hornfelsic to granofelsic texture. Sample ST1108B experienced extensive partial melting at shallow conditions (without strain) and is interpreted to be from zone 3 of the complex (Rubatto et al., 2006).

Figure1 : Map of Australia and New Zealand showing sample locations

c. Melt fluxed high strain shear zone:

To study the microstructures in a rock that has undergone melt fluxing during high strain deformation characteristic samples are chosen from a melt present shear zone in the Pembroke Granulites, Fiordland, New Zealand (Fig. 1). The samples PV1208-2, PV1420H, PV1430H were collected by Dr. Cait Stuart (MQ University) during her Ph.D. The gabbroic protolith of these granulites got partially recrystallized during a D1 event under a confining pressure of 11kbar (Stuart et al., 2016). The general description and microstructural observation of this melt bearing shear zone (<5% volume of melt) is provided in (Stuart et al., 2018). The deformation is closely associated with high Sr/Y magma implacement (D2) (Hollis et al., 2004; Allibone et al., 2009). Both the partially hydrated S1 foliation (by melt) and the D2 dykes of melt were hydrated during a second occurnace of porous melt flow (Stuart et al., 2017). This second melt flow event was driven by buoancy (during pre- and early D3), and hence synchronous with D3 deformation (Stuart et al., 2017). The samples PV1430H and PV1420H were collected from one of these intermediate to high strain zones. They thus represent porous melt flow in a shear zone. Another sample PV1208-2 was collected from the low strain domain of the shear zone, with felsic dykelets that has cut across the high strain S3 foliation. Hence this represents grain boundary melt flow in a nearly

static condition. This low strain sample is used here as a proxy to the monzogranite and to verify the nature of melt in a low-strain domain (Tab. 3).

Table. 3 *Sample geological history and field relationships*

Sample	*Approximate range of melt percentage*	*Quartz%*	*External differential stress during melt presence*	*Geological setting*	*Relative cooling rate*
Slow crystallizing static granitoid (Monzogranite) (W0809A)	*100—0%*	*33%*	*Low*	*Arc setting*	*slow*
Statically heated and cooled migmatite (ST1108B)	*< 10%*	*15%*	*Low*	*Regional aureole*	*slow*
Dynamic (syntectonic) migmatite (WJ1650A)	*<5%*	*8%*	*High*	*Regional aureole*	*fast*
Melt fluxed high strain shear zone (PV1208-2, PV1420H, PV1430H)	*<5%*	*5%*	*High*	*Arc setting (porous melt flow in high strain domain)*	*fast*
Quartz from an aqueous fluid in a Hornfels (AQ-4)	*0%*	*1%*	*Low (aqueous fluid)*	*Contact aureole*	*fast*

d. Quartz crystallizing from an aqueous fluid:

The very fine grained sample AQ-4 comes from the contact aureole of a Granite in the Lachlan Fold Belt at Jerrangle, NSW, Australia (Fig. 1). The samples' assemblage is andalusite-biotite-quartz which is typcial for a hornfels formed by metamorphic recrystallization at subsolidus conditions (Spear and Cheney, 1989). No synmetamorphic deformation event is reported from the area; hence this sample represents quartz crystallized at pores from an aqueous fluid under low stresses and in subsolidus conditions (Tab. 3).

Chapter 4: Results

I) General petrography:

a) Sample representing slow crystallization from a melt, low stress environment (W0809A)

The Rockvale monzogranite (W0809A) consists of K-feldspar-quartz-plagioclase-biotite-opaque ± garnet-muscovite and shows unimodal grain size distribution of quartz-plagioclase-K-feldspar (Fig. 2a, b). Primary magmatic features are well preserved including impingement of constituent grains at varying angles, overlapping of grains as a response to magmatic flow (Tab. 1, Fig. 2c, yellow arrow). Large phenocrysts of plagioclase and K-feldspar (close to 2mm across) are seen sharing boundaries sometimes with large quartz
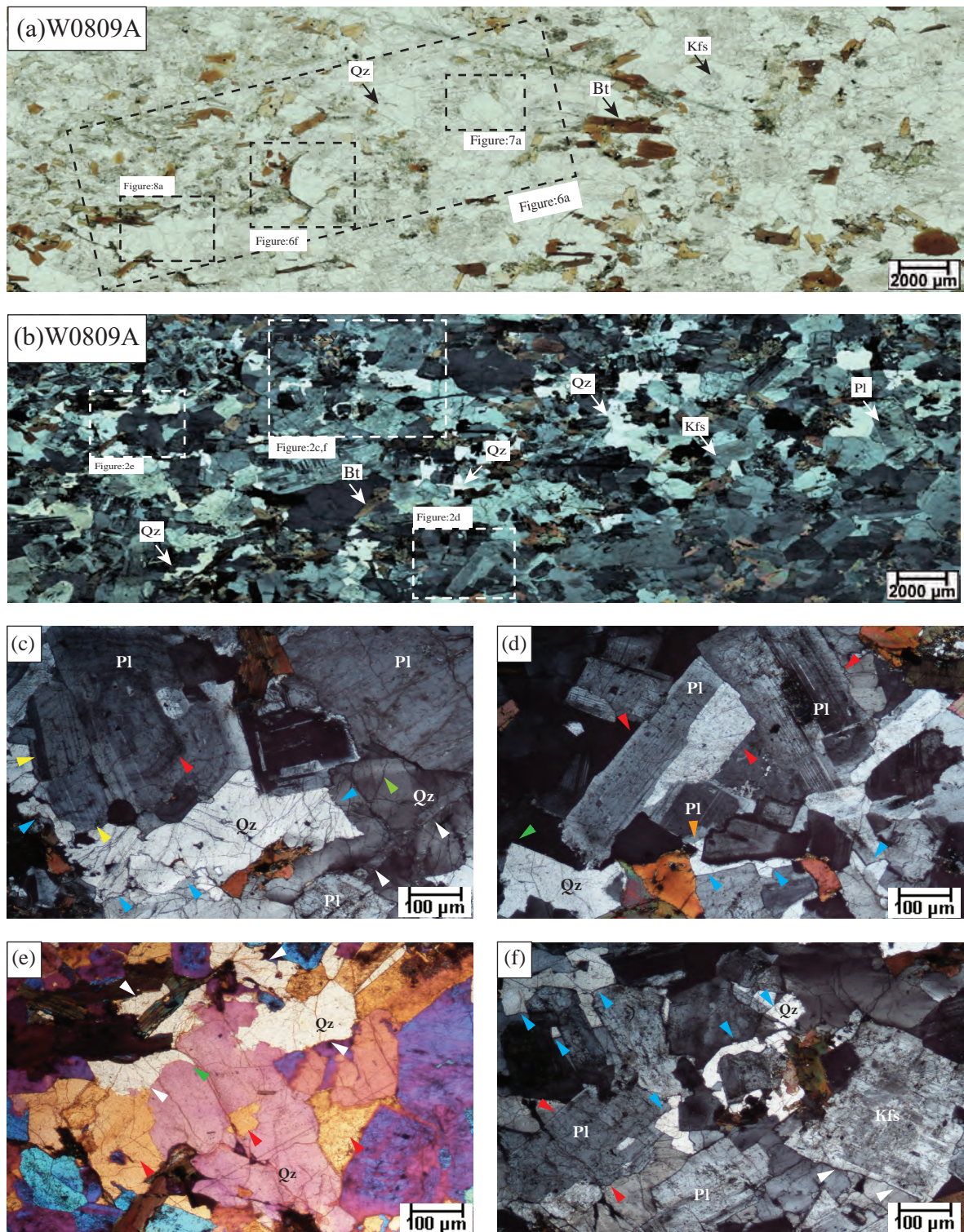
Figure 2: Photomicrographs of a monzo-granite collected from the Rockvalle Adamelite, Wongwibinda Meta. Complex (WMC)
a) Photomicrograph presenting the whole rock in Plane polarized light (PPL) b) Photomicrograph in XPL, shows the overall unimodal grain size distribution of quartz-plagioclase-Kfs. Biotite does not show any characterstic foliation (even locally). c) At the central left, Plagioclase feldspar shows concentric oscillatory zoning (red arrows) with two other feldpsar grains on its left (yellow arrows) discerning magmatic flow and colascence of grains. An irregular quartz grain (blue arrows) surrounds these grains. Undulose extinction of quartz can be seen at the lower right corner (green arow), also the grain cuts across by a plagioclase rich vein (white arrows) d) Plagioclase rich upper part with interstial quartz (blue arrows) forming an irregular shape, note the grain boundaries in plagioclase clusters are planer and parallel to the growth faces (examples are arrowed). Palgioclase grains are elongated. At the centre quartz grain shows low diehdral angle relationship with other plagioclase grains (orange arrow). The quartz grain has developed straight facted grain boundary (green arrow).
e) Photomicrograph taken with accesory plate of λ= 150nm, the quartz grains are connected in 3D as shown by the same interference colour (arrows having same colour). The left quartz grain has a cuspate shape. f) Irregular Quartz grains connected in 3D and go to extinction together (blue arrows). Note the euhedral shape Kfs at the lowewr right corner (white arrows). The plagioclase grain at the lower left corner (red arrows) shows planer grain boundary on one side and irregular boundary shared with quartz on the other.

16

grains with irregular boundaries and sometimes with small interstitial quartz grains having xenomorphic shape. Undulose extinction in some quartz grains can also be seen (Fig. 2c, green arrow). Quartz show well-developed crystal faces where they grew with more space (Fig. 2d, green arrow). Euhedral elongated crystals of plagioclase with concentric zoning and planer growth surfaces is observed (Fig. 2c, d). Low dihedral angle relationships between plagioclase-quartz-plagioclase can be seen (Fig. 2d, orange arrow). Quartz grains connected in 3D are found by inserting the accessory plate and a similar interference colour is identified (Fig. 2e, white arrow) or when the minerals go to extinction together (Fig. 2f, blue arrow). Potassium feldspar exhibits well-developed crystal faces representative of a crystal growth in a melt (Fig. 2f, white arrow). Features that are typically interpret as indicative of subsolidus deformation (or solid state flow) (Tab. 2) are absent. For example, long grains with undulose extinction, bimodal grain size distribution, core-mantle structures, ribbon quartz and asymmetric myrmekite at the edges of feldspars are missing. In addition, no foliation and kinking in biotite can be seen.

b) Statically heated and cooled migmatite from Mount-Stafford (ST1108B)

The sample ST1108B contains biotite-K-feldspar-quartz-cordierite-plagioclase-sillimanite-andalusite-ilmenite. The rock has a unimodal grain size appearance (Fig. 3a). K-feldspar dominates the overall assemblage (~55 vol. %), and are coarse, euhedral and close to 1mm across. Cordierite occurs as discrete grains and are between 0.5-0.8mm in size. Quartz is crystallized as an interstitial phase and possess straight faceted angular apperance (Fig. 3b, green arrow) sometimes with irregular notches resembling melt pseudomorphs. Hence, these melt films have wetted the grain boundary of reactant K-feldspar and cordierite. Sometimes the reactant minerals show irregular boundaries (Fig. 3b, red arrow). Melt inclusions and low dihedral angle (LDA) relationships can be seen (Fig. 3c, blue arrow). The interconnected nature of melt pockets can be seen in the quartz-rich part, by inserting the gypsum plate (Fig. 3d, white arrows). All these features are typical of crystallisation of partial melt under low stress environments (Tab. 1).

c) Dynamic (syntectonic) migmatite from Wongwibinda Metamorphic Complex (WMC)

The sample WJ1650A contains quartz-biotite-K-feldspar-cordierite. The rock is a fine grained variety and has bimodal grain size distribution with K-feldspar and cordierite forming larger grains (0.3-0.5mm across) and quartz forming smaller grains (<0.3mm). A pervasive foliation is defined by the alignment of small biotite grains. Sometimes they anastomose and surround the augens (Fig. 3e, red arrow). Areas of melanosome and leucosome can be well deciphered. Light coloured coarse-grained aggregates are identified
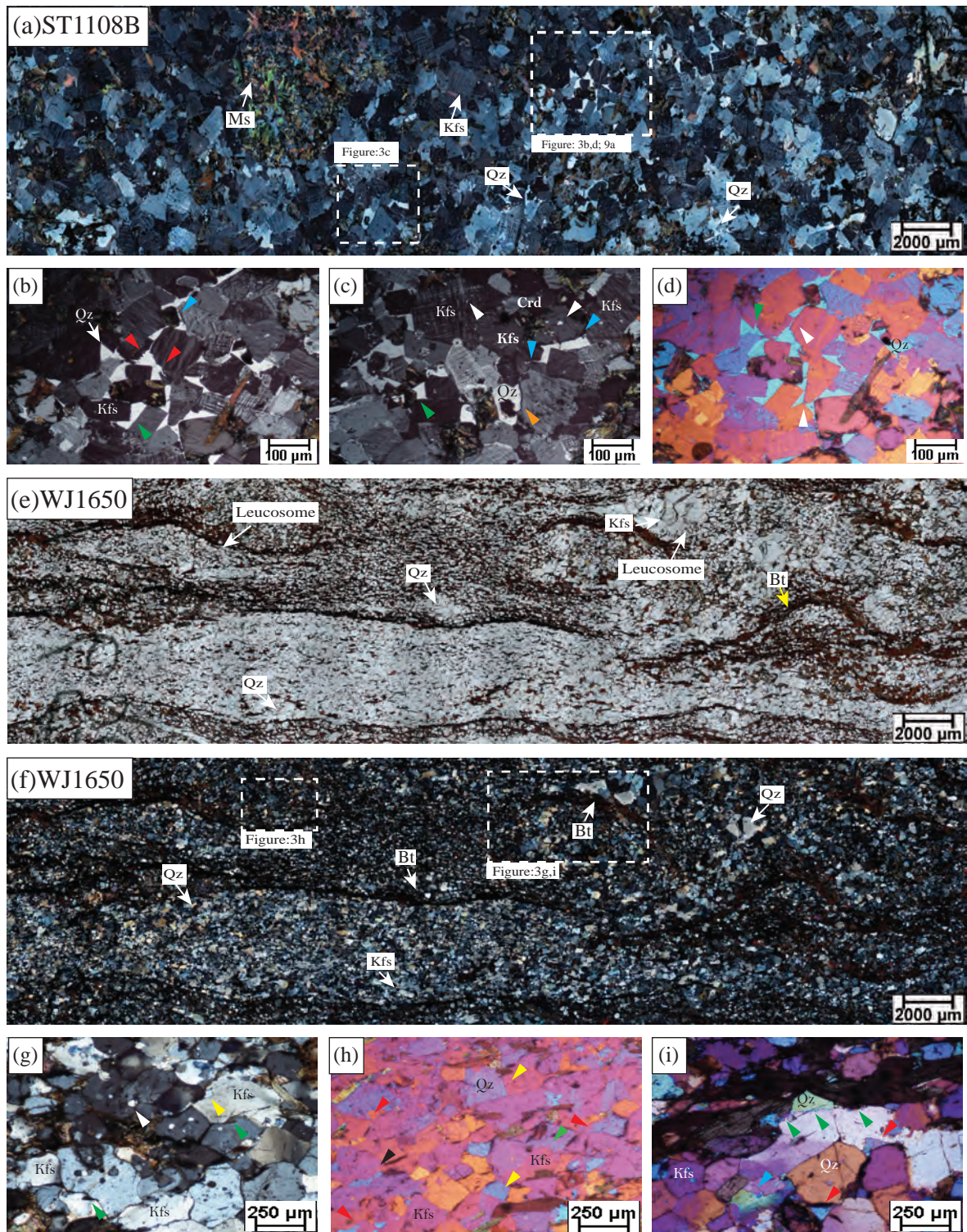
Figure 3: a) Photomicrograph of static migmatite ST1108B, collected from Mount Stafford, shows overall unimodal grain size in XPL. Inset shows area of EBSD mapping.b) The felsic melt crystallized as interstitial quartz grains.Note the straight faceted grains of quartz (green arrow), irregular xenomorphic quartz grain (blue arrow), and the reactant grains with corroded boundaries due to partial melting (red arrows). c) Area with less interstitial melt shows blocky nature of the single quartz grain pseudomorphing a melt pocket (green arrow). The melt inclusion is shown by white arrow. The low dihedral angle (LDA) relationship of interstitial quartz with orthoclase, as shown by blue arrows. An xenomorphic quartz grain is displayed by orrange arrow. d) Same area as shown in 'b' but with a λ= 150nm accessory plate. It shows the interconnected nature of the melt pockets wetting the grain boundaries of reactant minerals (white arrows). The interconnected melt-channel suggest the melt fraction was beyond MCT. A pointed edge of a quartz grain is seen pseudomorphing melt. e) A sample of dynamic migmatite taken from a shear zone in Wongwobinda metamorphic complex (WMC). The PPL photomicrograph displays a pervasive foliation developed by biotite, and patches of leucosomes parallel to this foliation. f) Same sample with XPL image. g) Photomicrograph of melanosome haiving reactant minerals. K-feldspars (Kfs) developing smooth cuspate shaped boundary with a very thin black lining. This is presumably melt, very fine to identify the composition. A single grain of quartzcan be seen crystallizing in that melt pocket (yellow arrow), White arrow shows melt inclusion. h) Blocky nature of quartz identifies areas of melt pocket (yellow arrows). LDA relationship at tripple junction can be seen (red arrow), and an xenomorphic quartz grain wetting the grain boundary of other minerals can be observed (black arrow). i) Interstial melt crystallized as blocky quartz grain with straight angular faces (red arrows), blue arrow shows evidence of partial melting, a thin melt film along the grain boundary could also be observed (green arrows)

18

as leucosome (Fig. 3f). Patches of melanosome show coarse K-feldspar grains with lobate boundaries. A very thin black film (in PPL) surrounding these boundaries is observed (Fig. 3g, green arrow). The composition of this film cannot be identified but presumably represents fine grained melt pseudomorphed products. Sometimes very small cuspate grains of cordierite/Kfs shares boundary with large K-feldspar (Fig. 3g, yellow arrow). Melt inclusions can also be observed (Fig. 3g, white arrow). Straight faceted blocky quartz grew with more space can be identified (Fig. 3h). Irregular xenomorphic quartz grains wetting the grain boundary are also identified. Low dihedral angle relationships of quartz with K-feldspar are seen. These features confirm the former presence of melt (Tab. 1). In some places, the quartz is crystallized as a melt pool forming very angular shapes with straight facets (Fig. 3i, red arrow) with a thin melt film at boundary (Fig. 3i, green arrow). Reactant grains have developed corroded grain boundaries as a result of partial melting (Fig. 3i, blue arrow).

d) Rocks from a melt fluxed shear zone, Pembroke Valley, New Zealand:

Three different types of rock samples are used; namely, PV1430H, PV1420H and PV1208-2. Of which, PV1430H and PV1420H comprises the high strain porous melt flow varieties collected from the shear zone and PV1208-2 is a low-strain domain sample with very low percentage of melt flux under nearly static conditions; it is collected adjacent to the shear zone. The high strain zone has an assemblage of magnesio-hornblende-clinozoisite-plagioclase-biotite-quartz-garnet-rutile (figure 4). Within the highly strained varieties the grain size varies depending on the spatial occurrence of the sample relative to the shear zone (compare the high strain varieties of Fig. 4a, b with Fig. 4c, d). SPO of tabular to prismatic magnesio-hornblende, biotite and quartz forms the D3 foliation, whereas the clinozoisite and plagioclase make up the fine grained matrix. At the resolution of the optical microscope, features commonly attributed to melt presence (see Tab. 1) are not identified. However, higher resolution BSE imaging show several features typical for melt presence. These include a. rounded quartz grains associated with xenomorphic plagioclase (Fig. 4e). Plagioclase grains filling up the triple-point and forms xenomorphic shape with cuspate boundaries (Fig. 4e, f). Stuart et al., 2018 concludes it as melt pseudomorphs. Let's term this as 'Type 1 melt microstructure' for this discussion, b. low dihedral angle between magnesio-hornblende-plagioclase-quartz and plagioclase-quartz-plagioclase (Fig. 4e, f, red arrows), c. polycrystalline multiphase aggregates of quartz-plagioclase-K-feldspar are seen at the triple junctions (Fig. 4g). Let's term this as 'Type 2 melt microstructure' for the discussion. All these features attribute to melt present deformation in a high strain domain (Tab. 1). The low
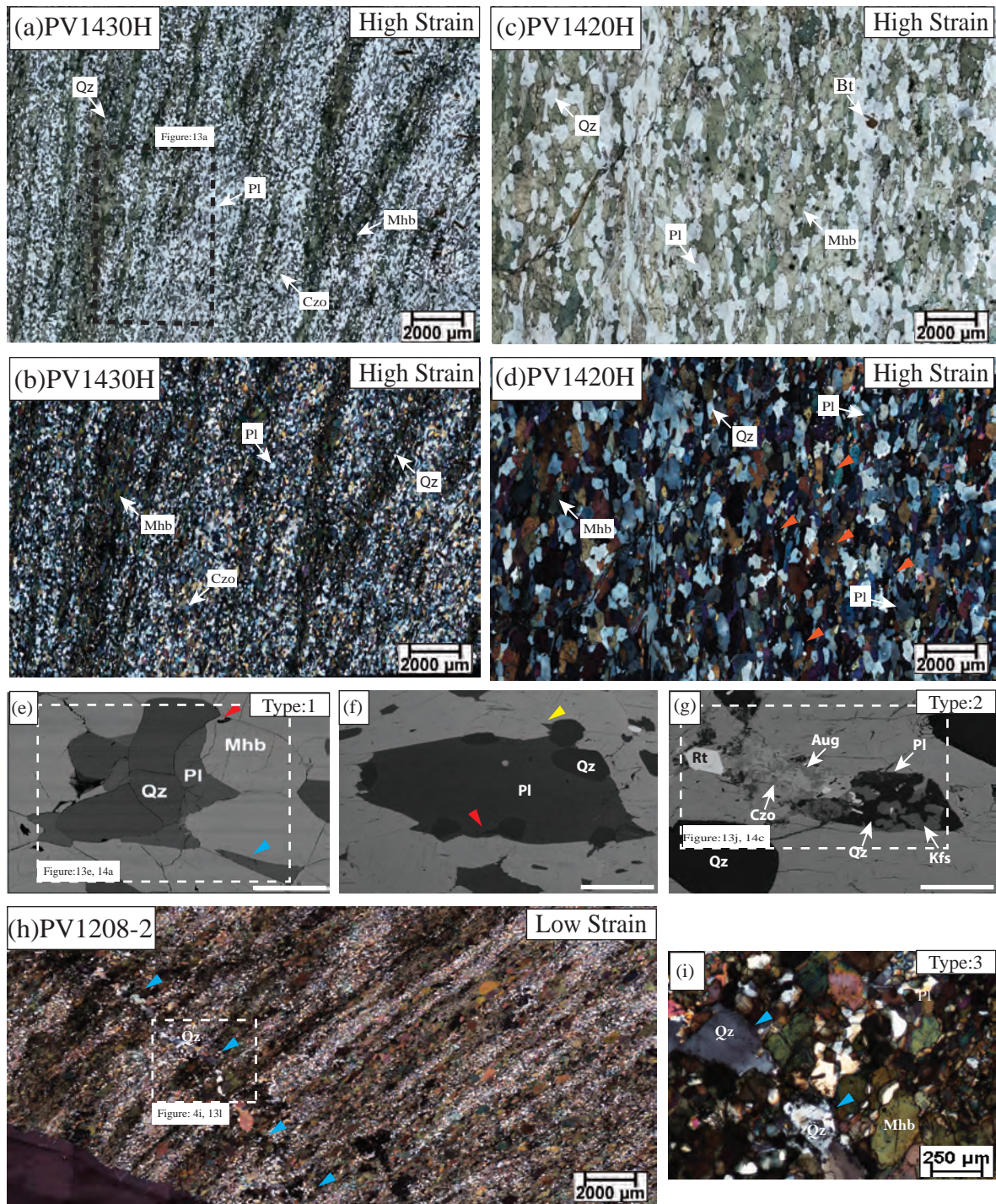
Figure 4: Photomicrograph of a rock from a melt fluxed shear zone in Pembroke Valley, New Zeland. Sample desription is given following Stuart et al., 2018. a & b) Photomicrograph of a high-strain domain in PPL and XPL respectively. Weak mineralogical layering can be seen with magnesio-hornblende+ quartz and plazioclase+cliozoisite. The area of EBSD map is shown in the box. c & d) A different rock sample, slightly away but within the shear zone, shown in PPL and XPL respectively. Note the overall unimodal grain-size distribution. Melt inclusions are marked in figure-'d' with red arrows. e-g) BSE image shows aggregate of plagioclase and quartz, crystallized from a melt. Scale bar shows 50µm.Note the low dihedral angles (LDA) are marked by red arrows. Also plagioclase has been crystallized as single phase in the interstices (blue arrow). Sharp pointed extension can also be observed (yellow arrow). In the figure-'g' aggregates of plagioclase+K-feldspar+quartz can be seen pseudomorphing a typical felsic melt pool. Here different features are marked as 'Type:1', 'Type:2' and 'Type:3' melt microstructure (refer to text). The square marks areas of EBSD mapping. h) Sample collected from a low-strain domain with felsic dykelets cutting across the foliation. This dykelet shows no feature of transportaion or modification by regional deformation. The inset shows area used for an EBSD map. i) Same area as shown in inset in figure- 'h', shows undulose extinction in crystallized quartz grains (blue arrows).

strain variety post-tectonic dykelet PV1208-2 cuts across the D3 foliations (Fig. 4f), and the mineralogy is dominated by quart and plagioclase, with minor hornblende+clinozoisite. Let's term this as 'Type 3 melt microstructure' for the discussion.

Petrography and microstructure of subsolidus rock under investigation:

e. Quartz crystallization from an aqueous fluid (AQ-4):

The rock AQ-4 comprises andalusite-biotite-muscovite-quartz, and shows bimodal grain size distribution. Biotite grains are dispersed and did not develop any characteristic foliations, typical of a hornfels (Fig. 5a, b). Andalusite grains are euhedral (Fig. 5c). The quartz grains have grown with interstitial textures, and show very minor undulose extinction (Fig. 5d).

II) Quantitative crystallographic orientation and WBV analysis:

a) Sample representing slow crystallization from a melt, low stress environment (W0809A)

The quartz grains (IPF_Z1 colour coded in Fig. 6a) show development of no CPO (Fig. 6b). Similarly, the plagioclase feldspars (Euler colour coding in Fig. 6c) show no preferred orientation for their constituent grains (Fig. 6d). Several features are observed: a) crystallized quartz grains display various shapes (elongated and equant) having sharp crystal boundaries (Fig. 6e), b) the grain size ranges from as small as 1.16×10^4 μm^2 to 7.73×10^4 μm^2 (Tab. 4), c) the dauphine twins (plotted in red contour in Fig. 6e) display enclosed continuous boundaries located as patches, and are mostly oriented along the edges, e) the subgrain boundaries having a misorientation range of 2°-5° and are spatially related to grain edges (fig. 6e; green arrow), f) very few >5° boundaries are seen. However, it is to be noted that these boundaries are optically invisible. Analysis on 'Grain2' and 'Grain4' (in Fig. 6f) display same 3D crystal orientation, and represent connected melt pockets. Misorientation profile shows change in crystal orientation up to 4-5° (Fig. 6g, h). And there is no consistency in misorientation/area for grains surrounded by different phases (Tab. 4). The textural component map (Fig. 6i, j) displays pronounced change in orientation along the grain edges. The local misorientation map also demonstrates the same with high population of 3° misorientation at the grain edges (Fig. 6k). The misorientation angle distribution histogram for the quartz fraction show disparity between correlated and uncorrelated data set at two places (Fig. 6l), one between 0°-5° and the other one between 55°-60°. The pole figure for the highlighted quartz 'Grain1' (devoid of any >2°/5° boundaries), shows no dispersion in pole figure (Fig. 6m), as we might expect for a grain growing under no actives stress in a granite. This grain has a dauphine density of 0.24. However, for most of the other
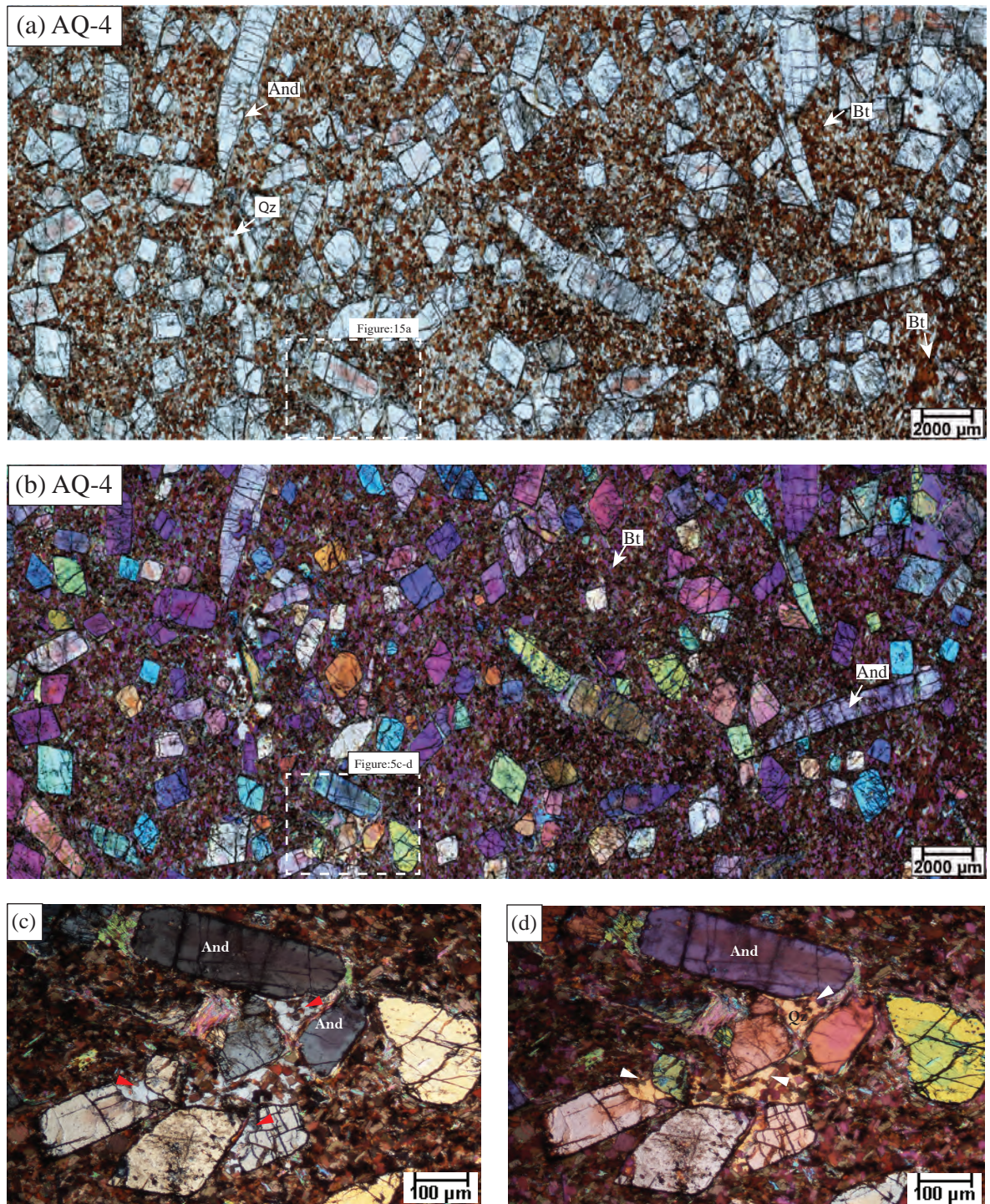
Figure 5: Photomicrographs of an andalusite-biotite-quartz hornfels collected from Jerangle, NSW, Australia and belongs to the Lachlan Fold belt. a) PPL photomicrograph shows pleochroic anadusite (And) and dispersed fine grained biotite. b) Same section in XPL. Note the random nature of andalusite crystals, inset shows the area from which EBSD map is taken c) same area as shown in inset (in the previous figure) where interstitial quartz (red arrows), crystallized from an aqueous fluid d) The similar interfearance colour with λ= 150nm accessory plate marks out a large grain of quartz in the groundmass

grains there is a range in pole figure dispersion, which varies from 5° to 28° (Tab. 4). 'Grain2' shows significant spread (17.09°, Tab. 4) in their lattice orientation (Fig. 6n). For the 'Grain3' two small scale dispersions (spread in disperion 15.35°, Tab. 4) are observed, and marked with '1' and '2'. 'Grain2' and 'Grain4' has dauphine densities of 0.021 and 0.29 respectively. Next two single quartz grains are analyzed (Fig. 7 and Fig. 8). 'Domain1', 'Domain2' and 'Domain3' are selected for the first grain since they comprise numerous subgrain walls (Fig. 7a). The whole quartz grain shows very disorganised pole figure responses for the a-axes (and 18° dispersion for c-axis), this may be due to the overalapping of dauphine twins onto each other (Fig. 7b). However, a faint two way dispersions can be identified for the a-axes and are marked with '1' and '2'. Inverse pole figure (IPF) also fails to show any strong prefreered orientation around a partcular crystallographic direction (Fig. 7c). Misorientation along a profile shows similar 4-5° change in crystal orientation (Fig. 7d). A vertical subgrain boundary trace for 'Domain1' (Fig. 7e) shows significant small scale dispersion for all the axes except for one of the a-axis (Fig. 7f). Hence, the rotation axis (R.A) is one of the <11-20> axes. The IPF for the same subgrain wall confirms this (Fig. 7g). The magnitude of WBV analysis is displayed by a conventional colour coding (Fig. 7h, Tab. 5). For 'Domain 1', a linear feature picks out the same subgrain wall with higher dislocation concentrations having WBVs of >0.002 μm^{-1}. The arrows are facing towards a particular direction (Fig. 7i). And a near single point clustering can be seen in the pole figure and in the IPF (Fig. 7j) for the same data set. The IPF shows a strong clustering around [c]. A schematic diagram (Fig. 7k) shows position of the orientation of different axes (as shown in Fig. 7f), also the rotational axis (R.A) is marked. The blue and green great circles show the reconstructed boundary plane orientation, if the boundary were a tilt wall and twist wall respectively. Clearly the subgrain boundary cannot be a twist wall, as it then will not conform to the observed boundary trace. Subgrain boundary plane is found to be (0001) plane. This plane defines a burger vector orientation (B.G) close to c-axis, similar to the observation made in the IPF of Fig. 7j. So an array of edge dislocations lying in the basal plane would be consistent with the determined subgrain boundary geometry. The misorientation axis can be explained by the activation of {10-10} [0001] slip system. A similar analysis for 'Domain2' on a horizontal subgrain boundary trace (Fig. 7l) shows misorientation axis as one of the <11-20> axes (Fig. 7m). And, the IPF shows a preferential crowding near to the prism planes. The WBV magnitude reads 4.80° (Tab. 5) with higher degree of dislocations, and the arrows are showing a particular direction (Fig. 7p). A schematic diagram is again prepared (7q), and a similar tilt wall approach is found to be

Figure 6: EBSD analysis on an undeformed monzogranite: W0809A with step size of 8μm (except 'figure:j,k'). a) Map shows whole fraction of quartz, with IPF_Z1 colour coding. The red lines show dauphine twins. Inset shows areas of further EBSD analysis. b) Quartz pole figures of crystallographic orientation (CPO) with one point per grain analysis (on the map of 'a'). c) Map of anorthite, with euler colour coding, having one point per grain. d) Anorthite CPO analysis on map of 'c'. e) Map shows BSE image of quartz, with anorthite-orthoclase assigned a particular phase colour. 2°, 5° and 10° boundaries are plotted (see legend). Note 2° subgrain boundaries (yellow) are populated close to the quartz-neighbour edges (green arrow). f) Orientation map of an area as shown in the 'a','e'. In all orientation map same IPF_Z1 colour scheme has been used (see the inset, on the right). Different grains are marked. Note the 'Grain2' and 'Grain4' has similar 3D crystal orientation measured at a refrence point '×'.These two grains are connected melt pockets. g-h) Change in crystallographic orientation, for 'Grain1' and 'Grain2', can be seen along 'AB' and 'CD' profile. Misorientation goes up to 4-5° measured from one end. i-j) Misorientation measured from a particular reference point '×' shows bending in crystal along the edges (white arrows). k) Map shows population of 3° misorientations along the grain edges. Grain edge is marked by fine black line (>10° boubdaries). Dauphine twin for quartz is also shown with red lines. Figure-'j','k' shows a map as shown in 'a' but with a smaller step size of 4μm. l) Misorientation angle distribution for the whole fraction of quartz shows disparity b/w correlated and uncorrelated data set at two places (marked with arrows, and one is highlighted in inset). m-o) Pole figures (stereographic, upper hemisphere) shows grain in colour of orientation map 'f '. 'Grain1' does not show small scale dispersion, whereas 'Grain2' shows dispersion in the c and a-axes. Grain3 shows significant small scale dispersion in two direction as marked by '1' and '2'.
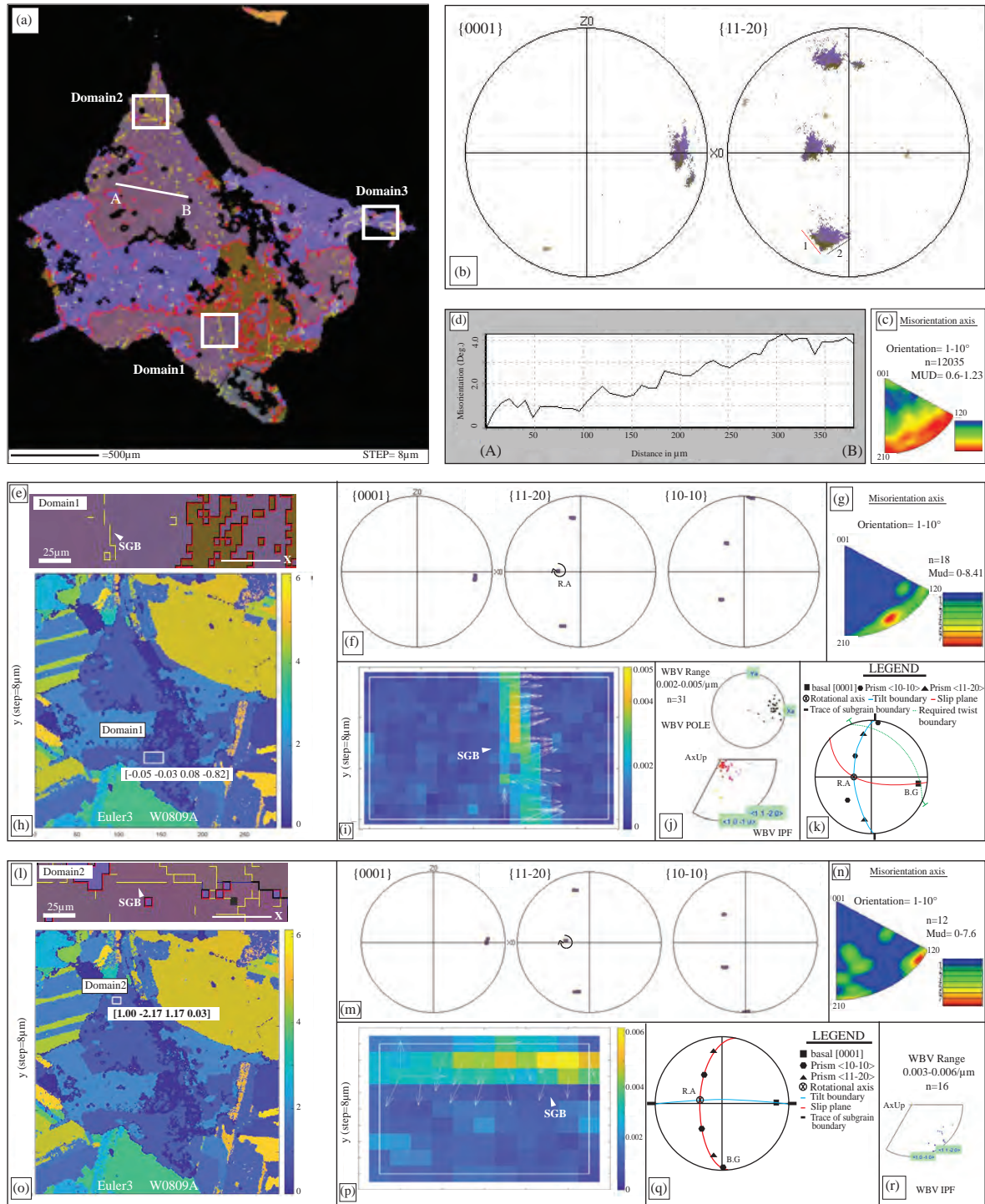
24

Figure 7: a) Map of a single quartz grain, as shown in figure: 6 a,e, here colour coded by Euler angles. The step size is 8µm . The grain shows population of 2° subgrain boundaries at grain edges. Different domains are shown for further EBSD analysis on these subgrain boundaries b) Pole figure (stereographic, upper hemisephere) for the whole grain depicts disorganized fashion. The two possible disper--sion is shown for the a-axes by '1' and '2' markings. c) Contoured inverse pole figure does not show any charactersitic development of rotational axis for 1-10° rotation. d) Misorientation along a profile 'AB' (profile is shown in 'a') shows change in crystal orientation upto 4°. e) Magnified region of 'Domain1', as shown in 'a', shows a vertical trace of the subgrain boundary (SGB) (arrowed) under consideration. f) Pole figure (stereographic, upper hemisephere) for 'Domain1' vertical subgrain boundary. Note the misorientation/ rotational axis where data do not show significant dispersion (arrowed). g) Contoured inverse pole figure showing rotational axis for same data set as in 'f'. h) WBV colour-coded magnitude map over the whole area shown in 'a'. The 'Domain1' is shown with weighted burger vector values parallel to the four axes of hexagonal quartz crystal. Note the WBV value parallel to the 'c' crystallographic direction is 10x higher than the rest (Table:3). i) The 3D WBV is projected ,onto the map of 'f' for 'Domain1', and marked as arrows. Only those with magnitude > 0.002/µm are shown with directions. j) Pole figure and inverse pole figure (IPF), for the same data set of 'Domain1' as shown in 'i'. Note the clustering of the WBVs. k) Pole figure (stereographic, upper hemisephere) to show schematically the position of the orientation of different axes and pole to planes, as shown in 'g'. The dispersion is not shown, although the interpreted rotational axis (R.A) and burgers vector direction (B.G) are marked (see text for details). l) A horizontal subgrain boundary trace (SGB) is marked on the magnified map of 'Domain2'. m) Pole figure (stereographic, upper hemisephere) for a horizontal subgrain boundary as shown in 'l'. The rotational axis is marked by an arrow. n) Contoured IPF pole figure for the same data set. o) WBV colour coded magnitude map, similar to 'h', but for 'Domain2' is shown. p) The 3D WBV is projected for 'Domain2'. Note horizontal SGB trace can be inferred having a higher degree of dislocations. q) Similar schematic diagram as shown in 'k', but here for 'Domain2'. r) IPF for the same data set as in 'p'.

25

consistent. In this case a subgrain boundary plane is coinciding with a prism plane {10-10}, and the misorientation axis can be explained by the activation of (0001) <11-20> slip system (Tab. 5). The burger vector direction and type, as postulated by the schematic pole figure (B.G in Fig. 7q) conforms to the analysed WBV IPF for the subgrain wall (Fig. 7r). Similar analysis on 'Domain3' (not shown here) shows another horizontal trace of subgrain wall (parallel to 'x' axis) with the activation of {11-20} [0001] slip system (Tab. 5).

Table. 4 *Various properties for random quartz grains for each rock sample derived from EBSD data. To quantify the crystal bending and change in crystal orientation for a single grain the maximum misorientation along profiles is measured and is divided by the grain area to assess the area control on crystal bending. The spread of <c> axes for a single grain is derived from pole figure lattice dispersions. Phases that surround the investigated grain are provided to allow assessment of crystal bending dependence on neighbourhood.*

Rock	Grain area (x10^4 μm²)	Max misorientation	Mis/area	Dispersion in pole figure	Surrounded by different phases (rough estimation)
W0809A	3.01	4.00°	1.33	NO	Pl (100%)
	3.37	1.90°	0.56	NO	Bt (50%), Qz (50%)
	6.30	4.00°	0.64	18.00°	Bt (17%), Qz (49%),Kfs(34%)
	4.25	3.80°	0.89	15.35°	Bt (13%), Qz (48%), Pl (39%)
	3.70	5.00°	1.35	17.09°	Qz (40%), Pl (60%)
	1.76	4.40°	2.50	28.00°	Qz (50%), Pl (50%)
	7.73	2.12°	0.27	12.53°	Qz (30%), Pl (70%)
ST1108B	9.60	5.50°	0.57	23.41°	Qz (33%), Pl (67%)
	1.23	3.20°	2.60	8.00°	Bt (13%), Qz (62%), Pl (38%)
	3.80	4.80°	1.26	17.00°	Qz (40%), Pl (60%)
WJ1650	8.42	4.00°	0.48	10.21°	Kfs (100%)
	1.81	3.60°	2.21	17°	Kfs (50%), Pl (50%)
	3.80	4.50°	1.26	17.00°	Qz (40%), Pl (60%)
	10.02	9.00 (Garin1)	0.89	25	Pl (27%), Qz (73%)
PV1430H PV1208-2	1.9	2°	1.05	NO	Qz (33%), Pl (67%)
	1.0	2.5°	2.5	5°	Qz (76%), Pl (24%)
	0.82	4°	4.87	12°	Pl (98%), Qz (2%)
	1.33	3.8°	2.86	17°	Pl (45%), Hbl (55%)
AQ-4	2.5	4°	1.6	8°	Qz (70%), Pl (20%), Bt (10%)
	2.4	3.8°	1.58	10°	Bt (100%)

Another grain has been analysed with a high resolution map (step size 4 μm), and similarly 'Domain4', 'Domain5' and 'Domain6' are chosen (Fig. 8a). The whole grain shows a disorganised pole figure dispersion (Fig. 8b). The domains on WBV magnitude map shows maximum values for K_c (Fig. 8c, Tab. 5). 'Domain 4' shows a diagonal subgrain boundary trace, oriented at 45° to the reference 'x' direction (Fig. 8d). The pole figure dispersion and the IPF identifies [0001] as the misorientation/rotational axis (Fig. 8e, 8f). The projected 3D WBVs (Fig. 8g) shows a characteristic direction with the IPF shows an array of basal edge dislocations (Fig. 8h). A similar subgrain boundary is observed in
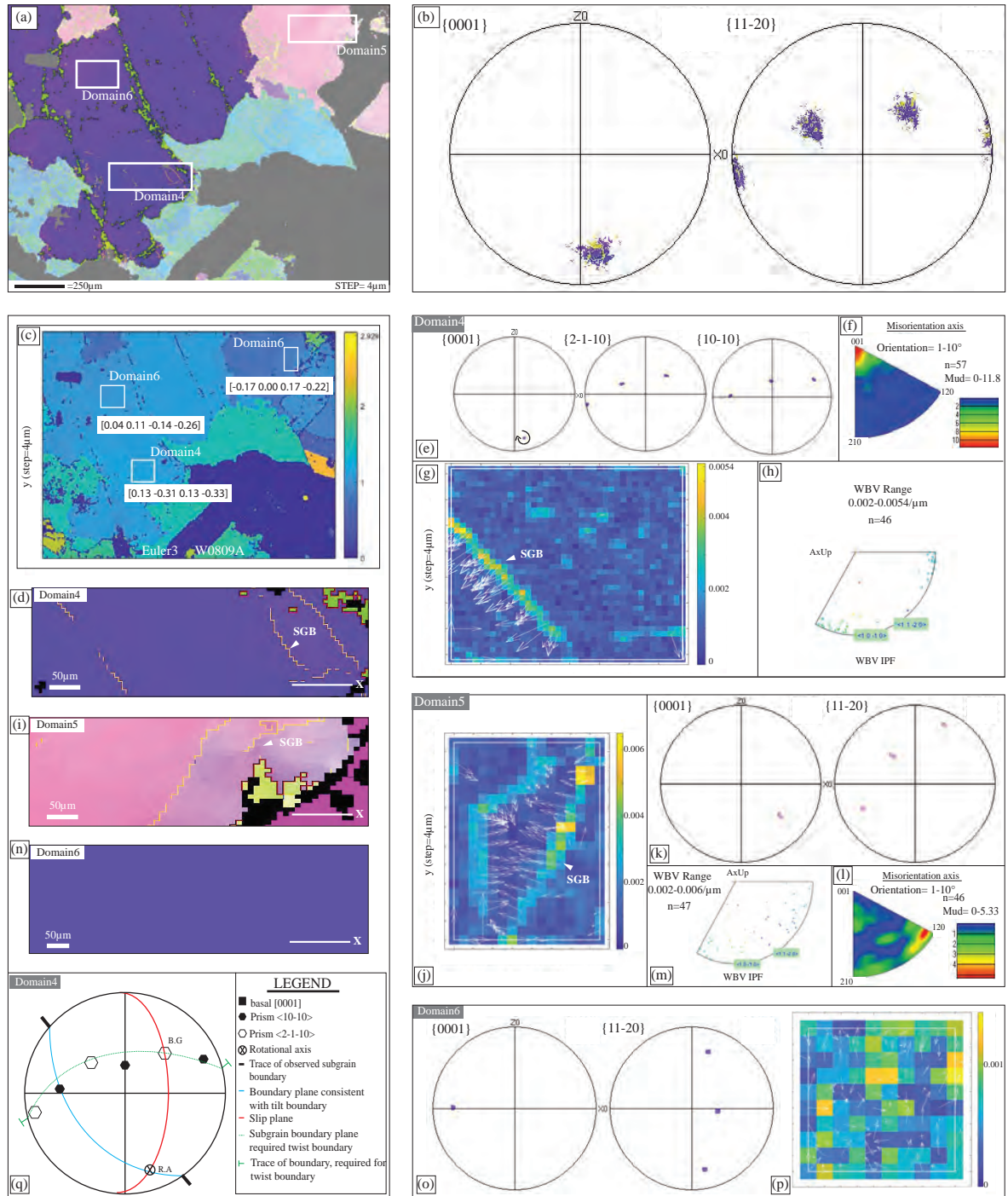
Figure 8: a) Map of a single quartz grain, as shown in 'figure: 6 a,j,k' here colour coded by conventional IPF_Z1 colouring. The step size is 4μm . Again different domains are shown for further analysis of subgrain boundaries as in 'figure: 7' b) Pole figure (stereographic, upper hemispehere) for the whole grain depicts disorganized fashion. c) WBV colour-coded magnitude map over the whole area shown in 'a' with same domains marked on it. d) Magnified region of 'Domain4' shows trace of the subgrain boundary (SGB) (arrowed) under consideration. e-h) Analysis made on 'Domain4' as shown on the EBSD orientation map (in 'a', 'd'), and on WBV orientation map in 'c'. e) Pole figure (stereographic, upper hemisphere) for one of the subgrain boundary. Note the misorientation,where data do not show significant dispersion (arrowed). f) Contoured inverse pole figure showing rotational axis for same data set as in 'e'. g) The 3D WBV is projected ,onto the map of 'c' for 'Domain4', and marked as arrows. Only those with magnitude > 0.002/μm are shown with a direction. The higher magnitude clearly depicts a subgrain boundary and conforms a similar morphology of SGB as shown in 'd'. h) Inverse pole figure (IPF), for the same data set of 'Domain4' as shown in 'g'. Note the clustering of the WBVs along the basal plane. i) Magnified region of 'Domain5' shows trace of subgrain boundary under observation. j-m) All the analysis made for 'Domain5'. j) 3D WBV colour coded magnitude map for 'Domain5' is shown. Notice the direction of subgrain boundaries are facing each other. k) Pole figure (stereographic, upper hemisphere) for the subgrain boundary as shown in 'i'. The rotational axis can not be identified as all the axes show dispersion. l) Contoured IPF pole figure for the data set shows the same. m) The IPF for 'Domain5' (for a range of 0.002-0.006/μm) shows points clustered along the basal plane. n) A 'Domain6' is chosen without any subgrain boundary trace. o-p) Analysis made on 'Domain6'. o) Pole figure (stereographic, upper hemisphere) does not show any small scale dispersion. p) The WBV directions are random and have a very small magnitude. q) Pole figure (stereographic, upper hemisphere) to show schematically the position of the orientation of different axes and pole to planes for 'Domain4', as shown in 'e'.The interpreted rotational axis (R.A) and burgers vector direction (B.G) (see text for details).

27

'Domain 5' (Fig. 8i), but displays a population of burger vectors directing towards each other (Fig. 8j). Pole figure dispersion shows dispersion in all the axis (Fig. 8k), and the IPF shows a random distribution for 1-10° orientation (Fig. 8l). A WBV IPF shows development of <c+a> dislocation type (Fig. 8m). 'Domain6' is devoid of any subgrain boundary (Fig. 8a, c, n), and does not display any characteristic dispersion in pole figure (Fig. 8o). Here, the length of WBVs reach only 0.0014 μm^{-1} (Fig. 8p) with a misorientation of mere 2.60° (Tab. 5). No clustering of WBVs can be seen towards a particular direction. A schematic diagram (Fig. 8q) for 'Domain4' shows an activation of {10-10} <2-1-10> slip system.

b) Statically heated and cooled migmatite from Mount-Stafford (ST1108B))

The whole quartz fraction (IPF_Z1 colouring, Fig. 9a) shows no preferred clustering (Fig. 9b). Similarly anorthite, with Euler colour coding (Fig. 9c), also displays no known trace induced lattice (or crystal) preferred orientation (Fig. 9d). A high resolution map (step size 5μm) shows several quartz grains with 2° subgrain boundaries populated at quartz-neighbour edges (Fig. 9e). Continuous dauphine twin boundaries are also seen associated with quartz edges (Fig. 9e), as seen in the monzogranite. 'Grain1' and 'Grain3' shows similar 3D crystal orientation (see inset on right), and identifies connected melt pockets. 'Grain2' has a slight change in crystal orientation compared to the previous grains. Two profiles 'AB' and 'CD' shows change in crystal orientation up to 4-5° (Fig. 9f, g). Also, there is no dependence of other phases on misorientation/area (Tab. 4). Also the 'Local misorientation' identifies higher degree of misorientation concentrated along the grain edges and at grain contacts (Fig. 9h). The textural component map also shows the same (examples arrowed) (Fig. 9i). Misorientation angle distribution for the whole fraction of quartz shows clear disparity at three places (marked in Fig. 9j). Pole figure dispersion for 'Grain1' in Fig. 9k shows disorganised fashion, except for [0001] axis (as marked by '1'). 'Grain4' shows dispersion in two directions as marked by '1' and '2' (Fig. 9l). Different domains are marked on Fig. 10a for subsequent subgrain boundary analysis. WBV magnitude map (Fig. 10b) shows length of WBVs parallel to different axis for these domains. The misorientaion for all the domains varies from 3.9° to as high as 6.32° (Tab. 5).

'Domain1' shows higher values of WBVs parallel to the a-axis, whereas in the 'Domain2' the highest value is associated with c-axis (Tab. 5). The pole figure and inverse pole figure show <11-20> as the misorientation axis (Fig. 10c, d) for the subgrain boundary in 'Domain1' (Fig. 10e). The 3D WBVs (Fig. 10f) figure out this boundary as a linear feature
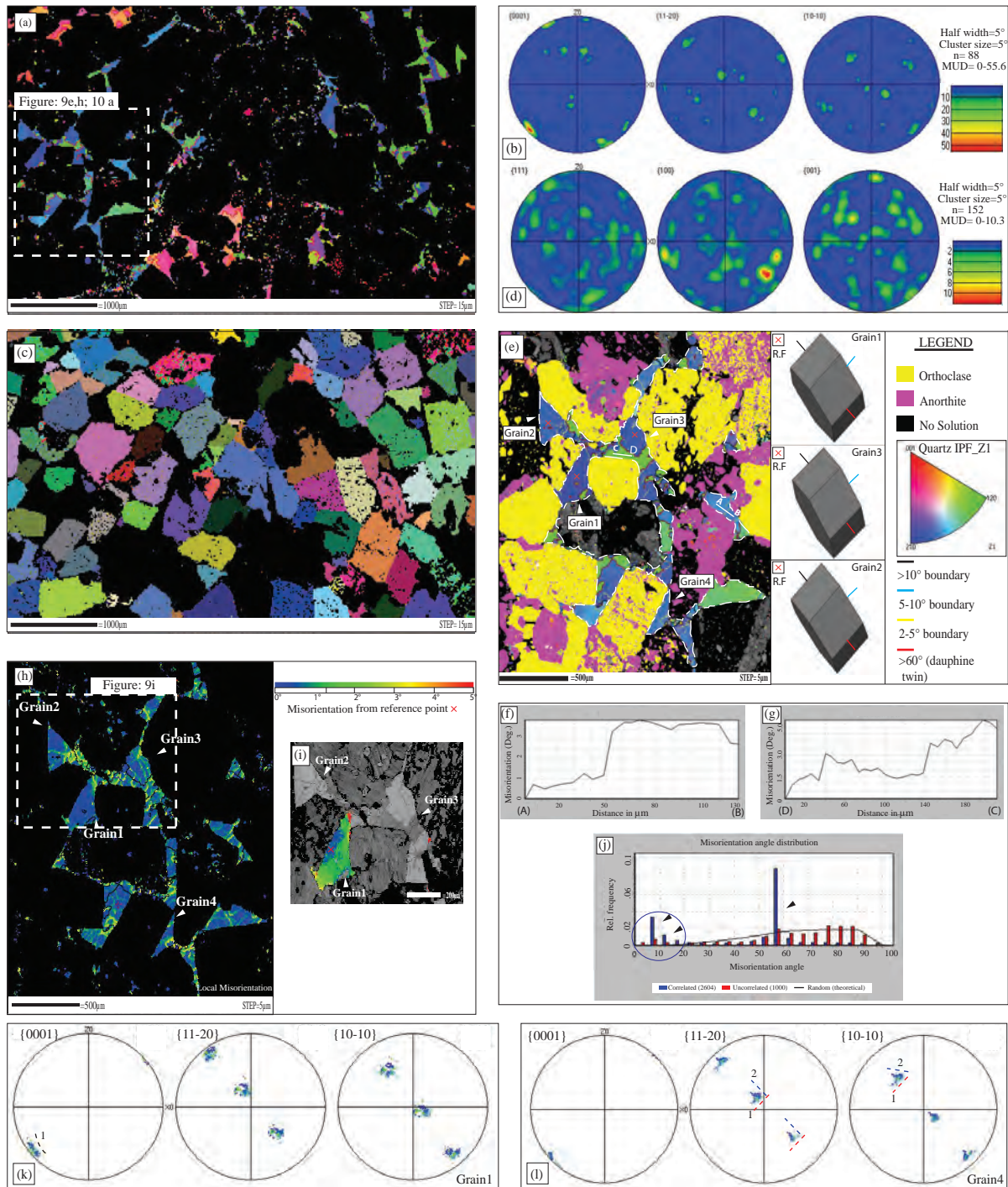
Figure 9: EBSD analysis on static migmatite: ST1108B with step size of 15µm (for CPO analysis) and 5µm for detailed analysis. a) Map shows whole fraction of quartz, with IPF_Z1 colour coding. One point per grain is taken for CPO analysis. Inset shows areas of further EBSD analysis. b) Quartz pole figures of crystallographic orientation (CPO) with one point per grain analysis (on the map of 'a'). c) Map of anorthite, with euler colour coding, having one point per grain. d) Anorthite CPO analysis on map of 'c'. e) Map (with step size of 5µm) shows BSE image with quartz assigned IPF_Z1 colour coding (marked by white dashed lines), and anorthite, orthoclase assigned particular phase colours as shown in legend. 2°, 5° and 10° boundaries are plotted. Note here also 2° subgrain boundaries (yellow) are populated close to the quartz-edges. Different grains are marked. Note the 'Grain1' and 'Grain3' has similar 3D crystal orientation. These two grains are connected melt pockets. Whereas 'Grain2' shows a small change in crystal orientation. f-g) Change in crystallographic orientation can be seen along 'AB' and 'DC' profile (marked in 'e'). Misorientation goes up to 4-5° measured from one end. h) Local misorientation measured for the whole quartz fraction shows higher concentration of 3° misorientation at quartz-neighbour edges and along grain boundaries.
i) Observed misorientation measured from a particular reference point '×' shows higher degree of misorientation away from grain interior (marked). j) Misorientation angle distribution for the whole fraction of quartz shows disparity b/w correlated and uncorrelated data set at two places (marked with arrows)for the low angle distribution. k) Pole figure (stereographic, upper hemisphere) shows grain in colour of orientation map 'e'. 'Grain1' shows single small scale dispersion of <0001> axis, whereas other axes are very disorganized. Grain4 shows significant small scale dispersion in two direction as marked by '1' and '2'.

29

with similar morphology shown in Fig. 10e. The pole figure, for the same data set, shows a clustering (Fig. 10g). And the IPF shows a concentration along the basal plane, specifically around <0-110>, which is pole to a prism plane.

Table. 5   *Integral WBVs taken for all the representative samples from specific areas (as 'Domains') in EBSD maps as shown in Fig. 7, 8, 10, 12 & 14. The step sizes and misorientation for the same data set are shown. The WBVs are decomposed parallel to the main four crystallographic axes and represented as K_{a1}, K_{a2}, K_{a3}, & K_c (following Wheeler et al., 2009). The inferred slip systems for each domain is shown with the type of dislocations representing subgrain boundaries.*

Sample Number	Step size (µm)	Domain	Misorie-ntation	K_{a1}	K_{a2}	K_{a3}	K_c	Inferred Slip system	Edge dislocation type
		1	3.05°	-0.05	-0.03	0.08	-0.82	{10-10} [0001]	[c]
	8	2	4.80°	1.00	-2.17	1.17	0.03	(0001) <11-20>	<a>
		3	3.27°	0.08	0.13	0.04	-0.76	{11-20} [0001]	<a>
		4	2.60°	0.13	-0.31	0.18	-0.33	{10-10} <2-1-10>	<a>
	4	5	4.61°	0.04	0.11	-0.14	0.26	NO	<a+c>
W0809A		6	2.60°	-0.17	0.00	0.17	-0.22	NO	NO
		1	6.32°	3.12	0.20	3.32	-0.55	(0001) <10-10>	<a>
	5	2	3.97°	1.19	-1.01	-0.19	-1.74	{11-20} [0001]	[c]
ST1108B		3	4.35°	3.61	-1.00	-2.61	-0.05	{01-11} <10-10>	<a>
		1	4.15°	1.02	-0.77	-0.25	-0.06	{11-20} <10-11>	<a>
	5	2	2.77°	-0.78	1.27	-0.49	-0.17	{01-11} <01-11>	<a>
		3	2.53°	-3.16	-2.05	-1.11	-0.07	{11-20} <11-20>	<a>
WJ1650A		4	3.38°	0.05	0.77	-0.82	-2.89	{10-11} [0001]	[c]
		1	0.81°	0.37	0.24	-0.62	-0.31	(0001) <01-10>	<a>
PV1430H	0.5	2	1.28°	1.68	-0.74	-0.94	-0.07	(0001) <10-10>	<a+c>
PV1420H	0.75	3	2.70°	0.90	0.36	-1.26	-1.98	NO	<a+c>
AQ-4	5	1	3.67°	-2.59	2.26	0.34	0.62	(01-11) <11-20>	<a>

A schematic pole figure diagram is drawn (Fig. 10i). And, the subgrain boundary plane is found to be consistent with a tilt boundary model and coincides with a prism plane. The estimated burger vector (B.G) is one of the <10-10> direction, and the observed slip system to describe this boundary wall would be (0001) <10-10>. Two other domains are similarly analysed. 'Domain2' pole figure dispersion and IPF contouring (Fig. 10j, k) for a near vertical subgrain wall (as shown in Fig. 10l) deciphers <11-20> as the rotation axis. The 3D WBVs pick out a portion of this subgrain wall (Fig. 10m) and shows a clustering around the [c] axis (Fig. 10n) as expected from the higher value correspond to K_c (Tab. 5). A tilt boundary model (not shown schematically for this domain) with a single type dislocation lying in a basal subgrain boundary plane with {11-20} [0001] slip system is deciphered
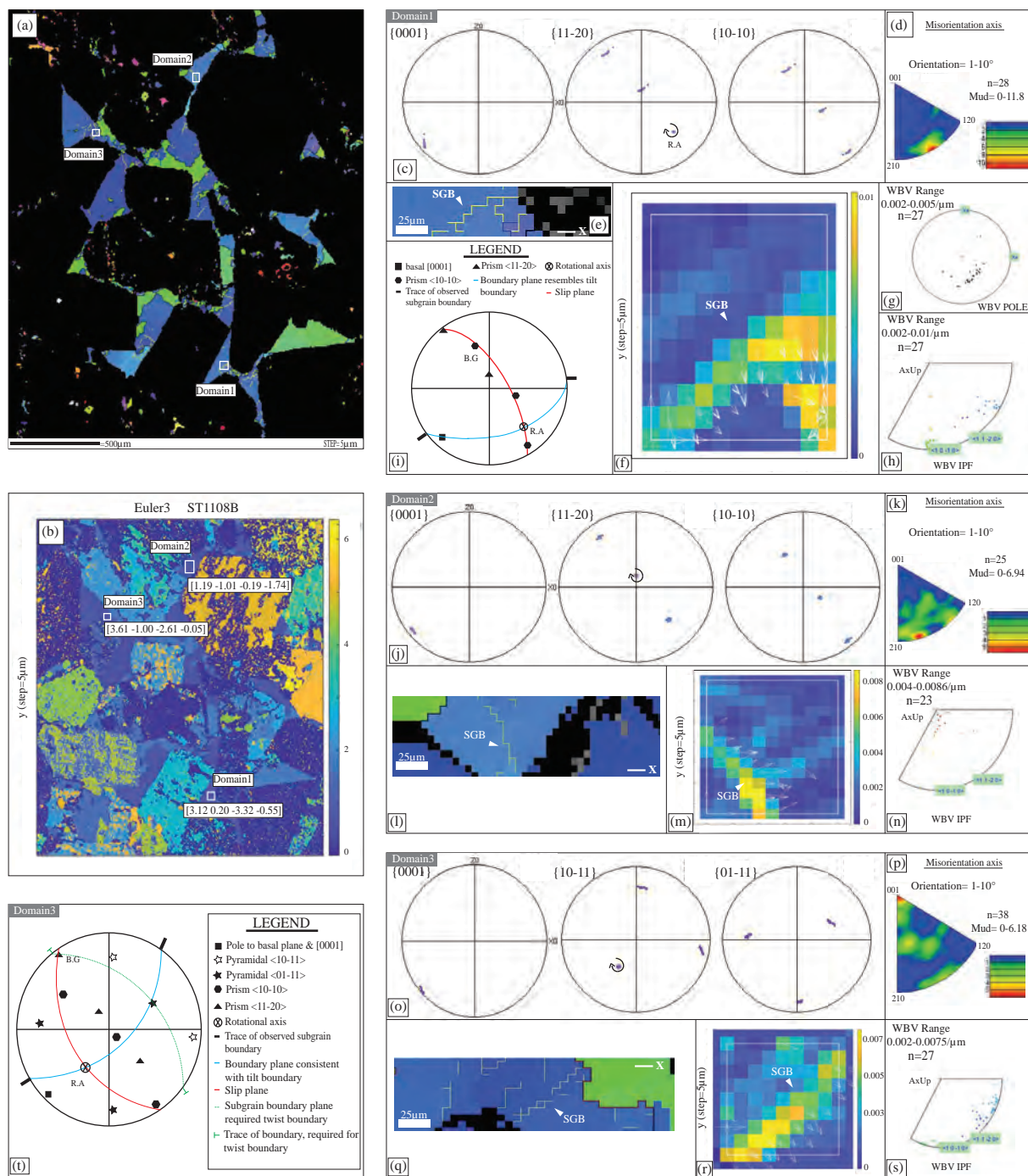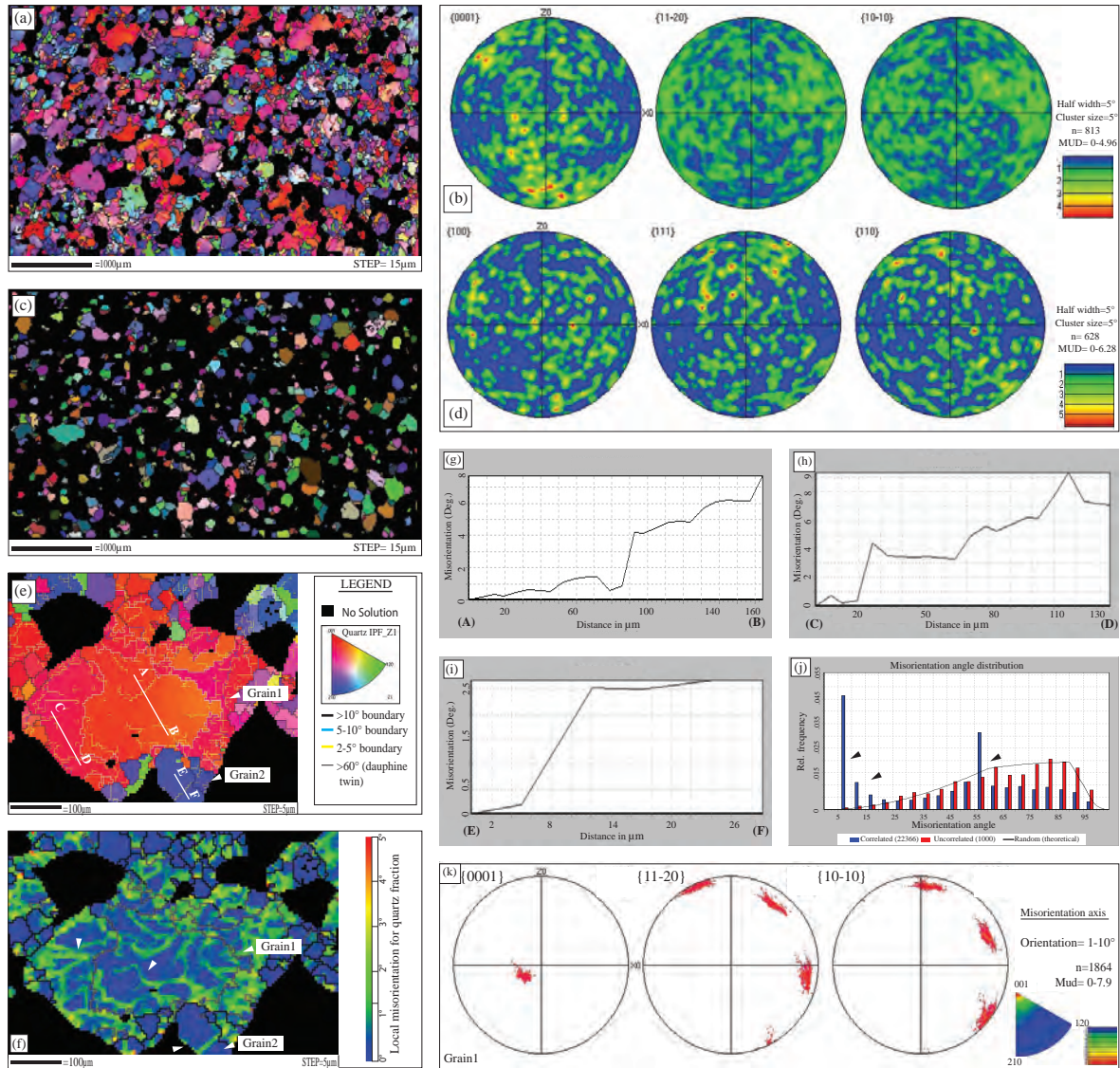
Figure 10: a) Map of quartz grains (IPF_Z1 colouring), having a step size 5µm, as shown in 'figure: 9e'. Again different domains are shown for further analysis of subgrain boundaries. b) WBV colour-coded magnitude map over the whole area, as shown in 'a', with different domains marked on it. c-h) Analysis made for 'Domain1' as shown on the EBSD orientation map (in 'a'), and on WBV orientation map in 'b'. c) Pole figure (stereographic, upper hemisphere) for 'Domain1'. Note the misorientation, where data do not show significant dispersion (arrowed). d) Contoured inverse pole figure showing rotational axis for same data set as in 'c'. e) Magnified region of 'Domain1'shows trace of the subgrain boundary (SGB) (arrowed) under consideration. f) The 3D WBV is projected ,onto the map of 'b' for 'Domain1', and marked as arrows. Only those with magnitude > 0.002/µm are shown with a direction. The higher magnitude deciphers a subgrain boundary with a similar morphology as shown in 'e'. g-h) Pole figure and inverse pole figure (IPF), for the same data set of 'Domain1' as shown in 'b' and 'f'. Note the clustering of the WBVs along the basal plane in IPF. i) Pole figure (stereographic, upper hemisphere) to show schematically the position of the orientation of different axes and pole to planes for 'Domain1' (as shown in 'c'). j-n) Analysis for 'Domain2'. j) Pole figure (stereographic, upper hemisphere) for 'Domain2' with misorientation axis (arrowed). k) Contoured inverse pole figure showing rotational axis for same data set as in 'j'. l) Magnified region of 'Domain2' shows trace of subgrain boundary under observation. m) The 3D WBV is projected ,onto the map of 'b' for 'Domain2', and marked with arrows for >0.004/µm. n) IPF for the same data set. o-s) Analysis for 'Domain3'. o) Pole figure (stereographic, upper hemisphere) for the 'Domain3'. The rotational axis is marked. p) Contoured IPF pole figure, for the same data set, does not show a preferred clustering. q) Magnified region of 'Domain3' shows trace of subgrain boundaries under observation. r) The 3D WBV is projected ,onto the map of 'b' for 'Domain3'. s) IPF for the same data set. t) Pole figure (stereographic, upper hemisphere) to show schematically the position of the orientation of different axes and pole to planes for 'Domain1', as shown in 'c'.The interpreted rotational axis (R.A) and burgers vector direction (B.G) (see text for details).

31

(Tab. 5). 'Domain3' pole figure dispersion identifies rotational axis as a pole to one of the pyramidal plane <10-11> (Fig. 10o) for a subgrain wall (as shown in Fig. 10q). A feeble clustering around the <r> axis supports this observation (Fig. 10p). The 3D WBVs trace a portion of the subgrain wall (Fig. 10r) with an array of edge dislocations lying on the prism plane (Fig. 10s). A schematic diagram (Fig. 10t) suggests a tilt model. A slip system with one of the {01-11} pyramidal plane as slip plane and one of the <10-10> direction as the slip direction is identified (Tab. 5).

c) Dynamic (syntectonic) migmatite from Wongwobinda Metamorphic Complex (WMC)

The whole fraction of quartz, with IPF_Z1 colour coding (Fig. 11a), shows no preferred orientation for the constituent quartz (Fig. 11b). Similarly plagioclase, with Euler colour coding (Fig. 11c), deciphers no CPO (Fig. 11d). Two quartz grains are marked as 'Grain1' and 'Grain2' (Fig. 11e). 'Gran1' is a large quartz grain with thick dauphine twins and lots of 2-5° subgrain boundaries appearing almost everywhere. 'Grain2' displays one 2-5° subgrain boundary at the grain edge, which cuts across the whole grain. The local misorientation shows higher degree of misorientation associated with 'Grain1' (arrowed, Fig. 11f), and a slight crystal bending can be seen at the grain edge for 'Grain2' (arrowed, Fig. 11f). Two misorientation profiles 'AB' and 'CD' for 'Grain1' (Fig. 11f) shows relatively higher change in crystal orientation and it reaches up to 9° (Fig. 11g, h).Whereas for the 'Grain2', 'EF' profile shows a change in crystal orientation of only 2.5-3° (Fig. 11i). There is no consistency for misorientation/area for grains surrounded by different phases (Tab. 4). Misorientation angle distribution for the whole fraction shows disparity between correlated and uncorrelated data set at three places (Fig. 11j, marked). An additional large mismatch correspond to 10-15° is seen. Upper hemisphere pole figure for the 'Grain1' shows dispersion in crystal orientation for the a-axes (Fig. 11k), and a strong [c] axis clustering can also be observed in IPF. This is different to our previous observations where no certain rotation axis for a 'whole single grain' was observed. Different domains are marked in Fig. 12a and also on the WBV magnitude map (Fig. 12b). Notice 'Domain1 to 3' shows higher values of WBV parallel to the a1, a2 and a3-axis, in comparison 'Domain4' shows higher value parallel to the c-axis (Tab. 5). Pole figure dispersion and IPF analysis (Fig. 12c, d) for a sub-horizontal subgrain boundary trace (Fig. 12e) for 'Domain1' shows development of one of the <10-11> axis as the rotational axis. However, the IPF (without contouring) shows distribution of points from close to [c] axis down to the base (Fig. 12d), and may be due to the error associated with small angle measurements (Wheeler et al., 2001).

Figure 11: EBSD analysis on dynamic migmatite: WJ1650A with step size of 15µm (for CPO analysis) and 5µm for detailed analysis.
a) map shows whole fraction of quartz, with IPF_Z1 colour coding. One point per grain is taken for CPO analysis. b) Quartz pole figures of crystallographic orientation (CPO) with one point per grain analysis (on the map of 'a'). c) Map of anorthite, with euler colour coding, having one point per grain. d) Anorthite CPO analysis on map of 'c'. e) Map (with step size of 5µm) shows quartz grains, assigned IPF_Z1 colour coding (true for all the analysis), and anorthite is assigned a particular phase colour as shown in legend. 2°, 5° and 10° boundaries are plotted. Note here 2° subgrain boundaries (yellow) are everywhere for the central quartz grain (marked as 'Grain1'). Where as in the grain below (marked as 'Grain2'), a 2° boundary starts from the grain edge protrudes inside. f) Local misorientation measured for the whole quartz fraction shows higher concentration of 3° misorientation at the grain interior for 'Grain1' (marked with arrows). Whereas 2.5° misorientation is observed at grain edge (and then cuts the grain across) (arrowed). g-h) Misorientation along profile 'AB' and 'CD' for 'Grain1' (profiles are shown in 'e') shows higher degree of change in crystal orientation, comapred to previous rocks. The observed misorientation goes as high as 9°.i) Misorientation profile 'EF' (shown in 'e') displays change in crystal orientation in the order of 2-3°. j) Misorientation angle distribution for the whole fraction of quartz shows a disparity b/w correlated and uncorrelated data set at three places (marked with arrows). Note a second disparity marks between 10-15°. k) Pole figure (stereographic, upper hemisphere) shows grain in colour of orientation map 'e'. 'Grain1' shows clear single small scale dispersion of a-axes. Also the contoured inverse pole figure shows development of strong rotational axis marked by <001> .

33

Projected 3D WBVs of >0.003μm^{-1} picks a linear sub-horizontal feature (Fig. 12f), and shows a clustering along the basal plane (Fig. 12g). Similar analysis for 'Domain2' picks a rotational axis as one of the <01-11> axis (pole to a pyramidal plane) (Fig. 12h). An IPF for the same data set confirms this (Fig. 12i). A diagonal subgrain boundary trace for this domain (Fig. 12j) can also be seen in the WBV magnitude map (Fig. 12k). And a clustering along the basal plane can be deciphered (Fig. 12l). In 'Domain3' the 'Grain1' shows [0001] as the rotational axis (Fig. 12m, n). The subgrain boundary trace, at a high angle to the reference 'x'-axis (Fig. 12o), can be identified when WBVs are projected in 3D (Fig. 12p). They show a population along the basal plane (for > 0.012 μm^{-1}) (Fig. 12q). A schematic diagram (Fig. 12r) for 'Domain3' with the observed rotational axis and burgers vector direction infers a tilt boundary model, and identifies one of the {11-20} plane as the subgrain boundary plane. A slips system of {11-20} <11-20> can be coined for this subgrain boundary plane. Similar analysis on 'Domain1' and 'Domain2' identifies slip system as {11-20} <10-11> and {01-11} <01-11> respectively having basal edge dislocations. 'Domain4' for the 'Grain2' shows development of one of the <01-10> (pole to a prism plane) as rotational axis (figure 12s). The EBSD IPF shows the same (Fig. 12t). A diagonal subgrain boundary trace (Fig. 12u) can be identified with 3D WBVs having a magnitude > 0.0025 μm^{-1} (Fig. 12v). The weighted burger vectors show clustering close to the [c] axis for this data set (Fig. 12w). Hence, an array of edge dislocations lying in the basal plane can be inferred. A schematic diagram (Fig. 12x) shows a tilt boundary model with (0001) as the constructed subgrain boundary plane. The observed burger vector direction in Fig. 12w matches well with the marked 'B.G' in the schematic diagram, and hence prove the efficacy of this method. Here a slip system of {10-11} [0001] with edge dislocations lying in the basal (0001) plane is found.

d) Rock from a melt fluxed shear zone, Pembroke Valley, New Zealand:

Quartz fraction with IPF_Z1 colouring (Fig. 12a, step size of 8 μm) shows no development of preferred orientation for any crystallographic axis (Fig. 12b). The Euler anorthite map (Fig. 13c) also shows the same (Fig. 13d). This is very hard to identify clearly the difference between a quartz grain crystallized from a melt and a quartz grain which is of the precursor rock, when they are both in a deforming (dynamic) environment optically. To avoid that confusion, only those quartz are taken into considerations that have had retained their magmatic microstructures. Hence the constituent quartz grains of those typical melt microstructures are analysed as described before. Orientation map of 'Type 1 melt
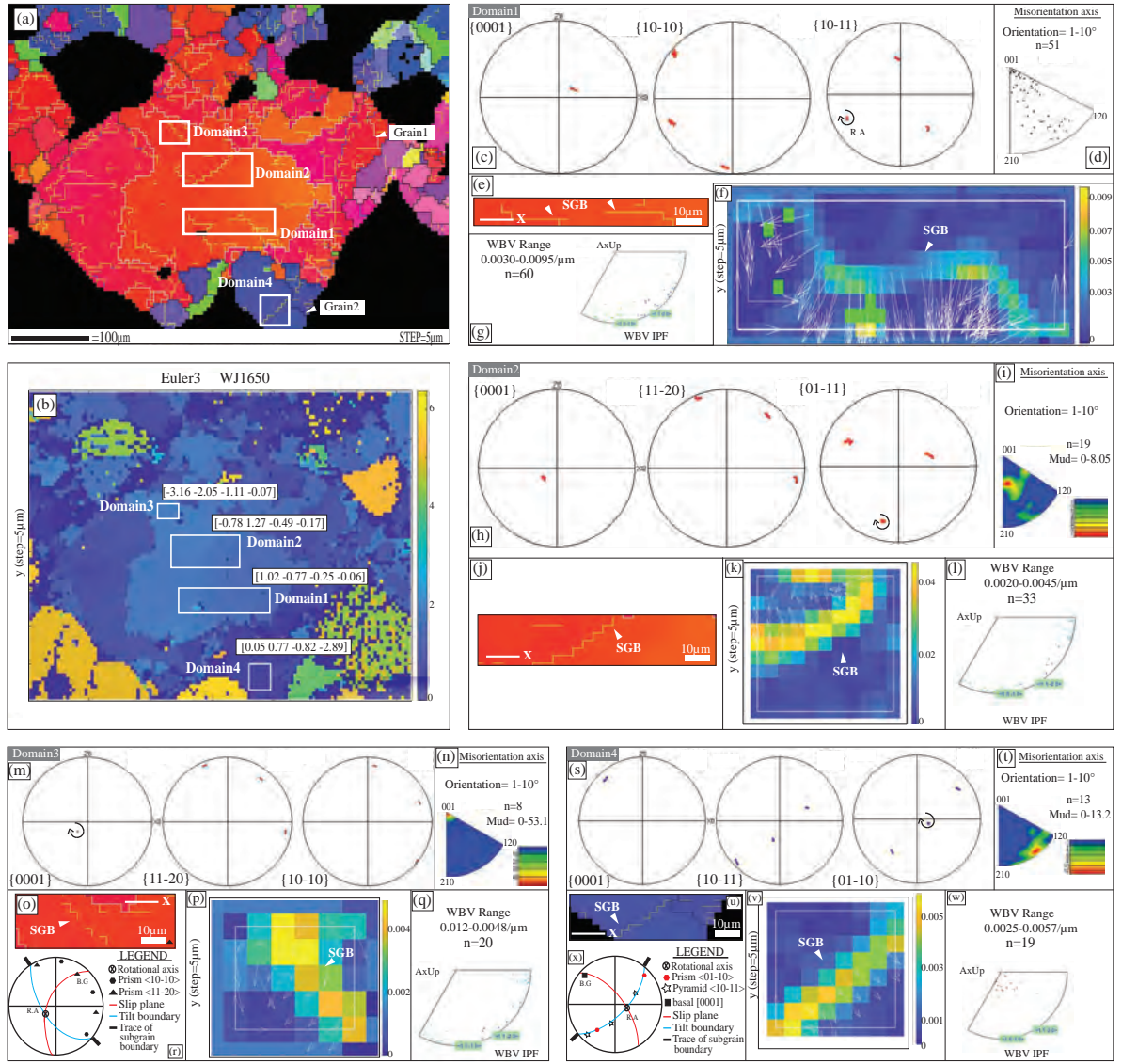
Figure 12: a) Map, as shown in figure: 11 e, here quartz is colour coded by conventional IPF_Z1 colouring. The step size is 5µm. Different domains are shown for further analysis of subgrain boundaries. 'Domain-1 to 3' are marked for 'Grain1' and 'Domain4' for 'Grain2'. b) WBV colour-coded magnitude map over the whole area, as shown in 'a', with similar domains marked on it. c-g) Analysis made for 'Domain1' as shown on the EBSD orientation map (in 'a'), and on WBV orientation map in 'b'. c) Pole figure (stereographic, upper hemisphere) shows the misorientation axis (arrowed). d) Inverse pole figure showing points for same data set as in 'c'. e) Magnified region of 'Domain1'shows trace of the subgrain boundary (SGB) (arrowed) under consideration. f) The 3D WBV is projected ,onto the map of 'b' for 'Domain1', and marked as arrows. Only those with magnitude > 0.003/µm are shown with a direction. The higher magnitude deciphers a subgrain boundary with a similar morphology as shown in 'e'. g) Inverse pole figure (IPF), for the same data set of 'Domain1' as shown in 'b' and 'f'. Note the clustering of the WBVs along the basal plane. h-l) Analysis for 'Domain2'. h) Pole figure (stereographic, upper hemisphere) for 'Domain2' with misorientation axis (arrowed). i) Contoured inverse pole figure showing rotational axis for same data set as in 'h'. j) Magnified region of 'Domain2' shows trace of subgrain boundary under observation. k) The 3D WBV is projected , onto the map of 'b' for 'Domain2', and marked with arrows for >0.002/µm. l) IPF for the same data set. m-r) Analysis for 'Domain3'. m) Pole figure (stereographic, upper hemisphere) for the 'Domain3'. The rotational axis is marked. n) Contoured IPF pole figure for the same data shows a preferred clustering around <001> (same as <0001>). o) Magnified region of 'Domain3' shows trace of subgrain boundary under observation. p) The 3D WBV is projected ,onto the map of 'b' for 'Domain3'. q) IPF for the same data set. r) Pole figure (stereographic, upper hemisphere) to show schematically the position of the orientation of different axes and pole to planes for 'Domain3'. The interpreted rotational axis (R.A) and burgers vector direction (B.G) are marked (see text for details). s-x) Analysis for 'Domain4'. s) Pole figure (stereographic, upper hemisphere) for 'Domain4' with misorientation axis (arrowed). t) Contoured inverse pole figure showing rotational axis for same data set as in 's'. u) Magnified region of 'Domain4' shows trace of subgrain boundary for 'Grain2' under observation. v) The 3D WBV is projected, onto the map of 'b' for 'Domain2', and marked with arrows for >0.002/µm. Note the similar morphology of subgrain boundary (SGB), marked with high magnitude of WBVs, and as seen in 'u'. w) IPF for the same data set. x) Pole figure (stereographic, upper hemisphere) to show schematically the position of the orientation of different axes and pole to planes for 'Domain4' (as seen in 's').

35

microstructure' (PV1430H, Fig. 13e) shows different quartz grains (in IPF_ZI colouring) with 2-5°, 5-10°, >10° subgrain boundaries. 2° subgrain boundaries are not observed in 'Grain1' and 'Grain2' (Fig. 13e). And 'Grain3' shows few 2° subgrain boundaries at the grain edge. Hence subgrain boundaries correspond to smaller misorientation of 0.7° are plotted. No dauphine twins are observed (Fig. 13e). Two profiles 'AB' and 'CD' display change in crystal orientation up to only 2-2.5° (Fig. 13f, g). This value is less compared to the observations made for the previous rocks (Tab. 4). Textural component map for different grains shows change in crystal orientation at the grain edges (Fig. 13h-i) in the order of 2-4°. Also the local misorientation map shows higher misorientation at the grain edge for 'Grain2' (Fig. 13i, arrowed). The 0.7° subgrain boundaries initiate at the grain edge and cut the whole grain across. 'Type 2 melt-microstructure' (PV1420H) shows relatively more 2° subgrain boundaries, and dauphine twins are also observed at the grain edges ('Grain4' in Fig. 13j). However, misorientation profile ('EF') shows change in crystal orientation only up to 2.5-3° at max (Fig. 13k). Hence both 'Type 1' and 'Type 2' melt microstructure shows relatively lesser change in crystal orientation (Tab. 4). 'Type 3 melt microstructure' (Fig. 13l) of a post tectonic dykelet shows change in crystal orientation up to 4° along a profile 'GH' ('Grain5' in Fig. 13m). Dauphine twins along the grain edges are also seen (Fig. 13l), similar to the monzogranite and static migmatite. Crystal bending is pronounced along the grain edges (Fig. 13o, marked with arrows). The misorientation angle distribution for the whole fraction of quartz shows disparity at two places (Fig. 13n). 'Type 2' quartz grain shows less dispersion in the pole figure (2-5°), when compared to 'Type 3' quartz grain (Fig. 13p, q; Tab. 4). But no particular rotational axis can be deciphered for both of them. In order to characterize the 0.7° subgrain boundaries two domains ('Domain1' and 'Domain2') are marked (Fig. 14a). Similarly, 'Domain3' is marked to characterise the 2° subgrain boundary (Fig. 14c). The WBV magnitude map shows these domains (Fig. 14d) with properties enlisted in Tab. 5. The misorientations associated with the fist two domains are less (in the order of 0.8-2.7°, Tab. 5) compared to the monzogranite and static migmatite. The pole figure dispersion for 'Domain1' shows <01-10> as the misorientation/ rotational axis (Fig. 14e). Also the IPF for the same data set confirms this (Fig. 14f). The 3D WBVs (> 0.011 μm^{-1}) for 'Domain1' displays a sub-horizontal boundary with all the burger vectors pointing downwards (Fig. 14g). For the same data set, WBV pole figure and IPF shows a clustering (Fig. 14h, i). Similar analysis on 'Domain2' marks <10-10> as the rotational axis (Fig. 14j). The projected 3D WBVs crosscut each other (Fig. 14k) with no definite direction. This nature can also be observed in the WBV IPF for the same data set (Fig. 14l) as there is no
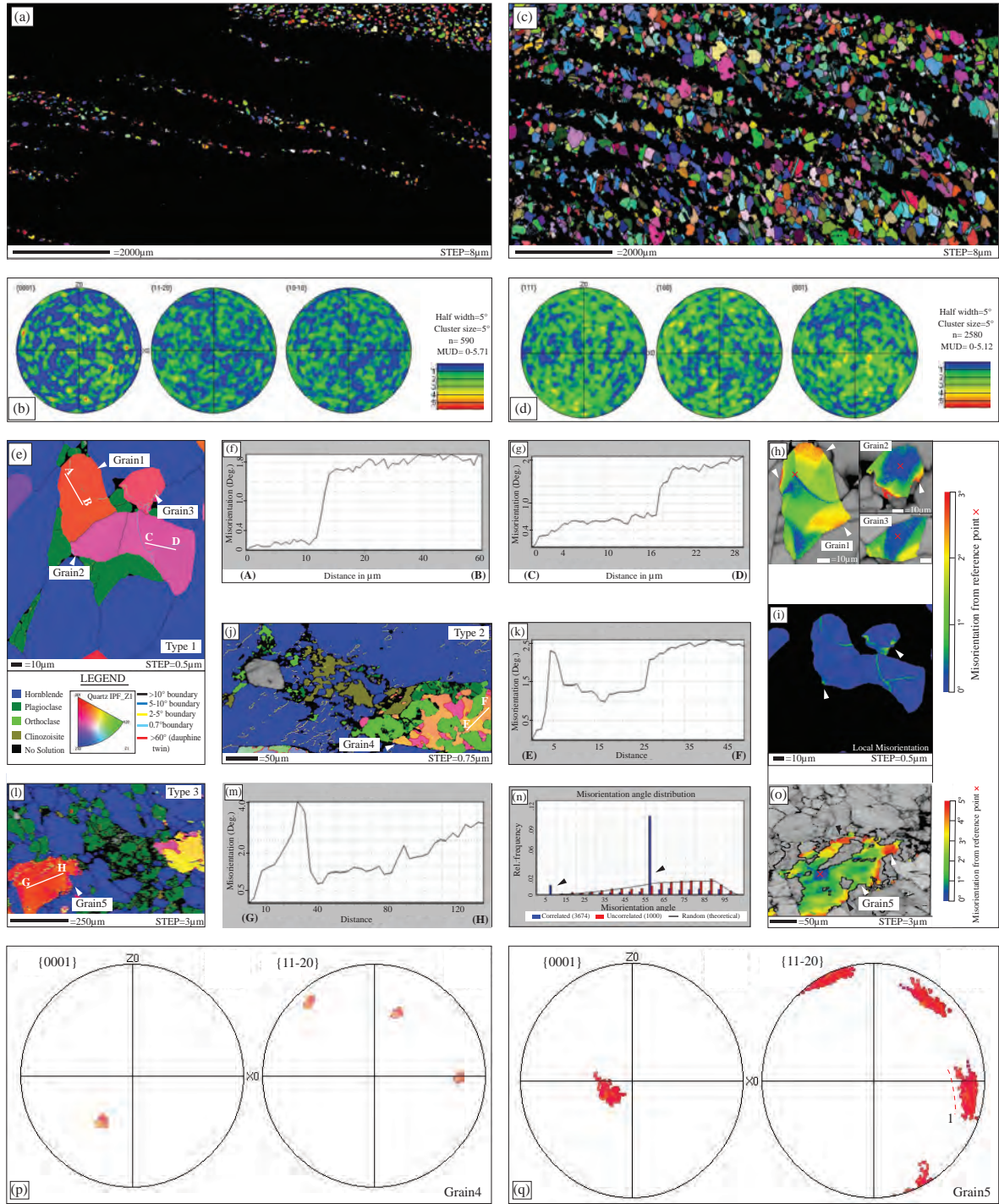
Figure 13: EBSD analysis on rocks from a melt-fluxed shear zone : PV1430H, PV1420H, PV1208-2. PV1430H with a step size of 8µm (for CPO analysis) and 0.5µm for detailed analysis. PV1420H with a step size of 0.75µm and PV1208-2 with a step size of 3µm for detailed analysis. a) map shows whole fraction of quartz, with IPF_Z1 colour coding. One point per grain is taken for CPO analysis. b) Quartz pole figures of crystallographic orientation (CPO) with one point per grain analysis (on the map of 'a'). c) Map of anorthite, with euler colour coding, having one point per grain. d) Anorthite CPO analysis on map of 'c'. e) Map (with step size of 0.5µm) shows quartz grains, assigned IPF_Z1 colour coding, and plagioclase-hornblende are assigned particular phase colours as shown in the legend. 0.7°, 2°, 5° and 10° boundaries are plotted. Note here 2° subgrain boundaries (yellow) are present at the grain edges of 'Grain3', and absent for the other grains. Whereas 0.7° boundaries are observed for the remaining grains. f-g) Misorientation along profile 'AB' for 'Grain1' and 'CD' for shows change in crystal orientation up to 2-3°. This is very less comapred to the previous observations. h) Textural component map shows crystal bending at the grain edges for all the grains, measured from a refrence point. i) Local misorientation measured for all quartz grains also shows higher population of misorientation along the grain edges. j) Another quartz grain in high strained sample PV1420H is observed. Here 2° subgrain boundaries are observed. k) misorientation along a profile 'EF' shows change in crystal orientation that reaches up to 3.5-4°. l) Quartz crystallized in a post tectonic dyklet is observed (see 'Chapter 4c'). m) Misorientation along a profile 'EF' shows change in crystal orientation up to 4-5°. n) Misorientation angle distribution for the whole quartz fraction (in 'a') shows disparity between correlated and uncorrelated data set. o) 'Grain5' (as shown in 'l') shows similar crystal bending along the grain edges. p) 'Grain4' does not show any characterstic small circle dispersion of the crystallographic axis. q) 'Grain5' shows strong dispersion at least along a single direction as shown by the '1'.
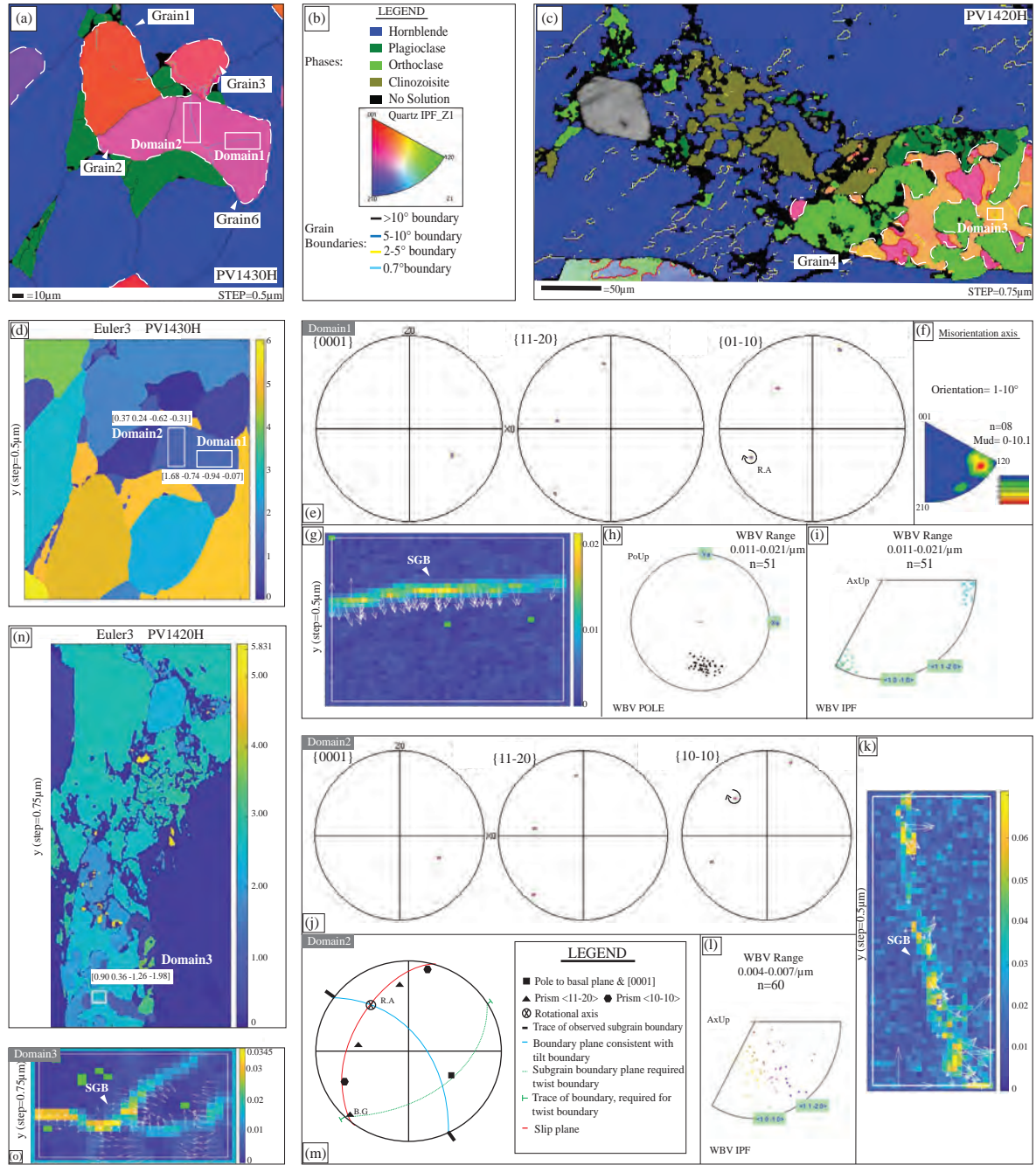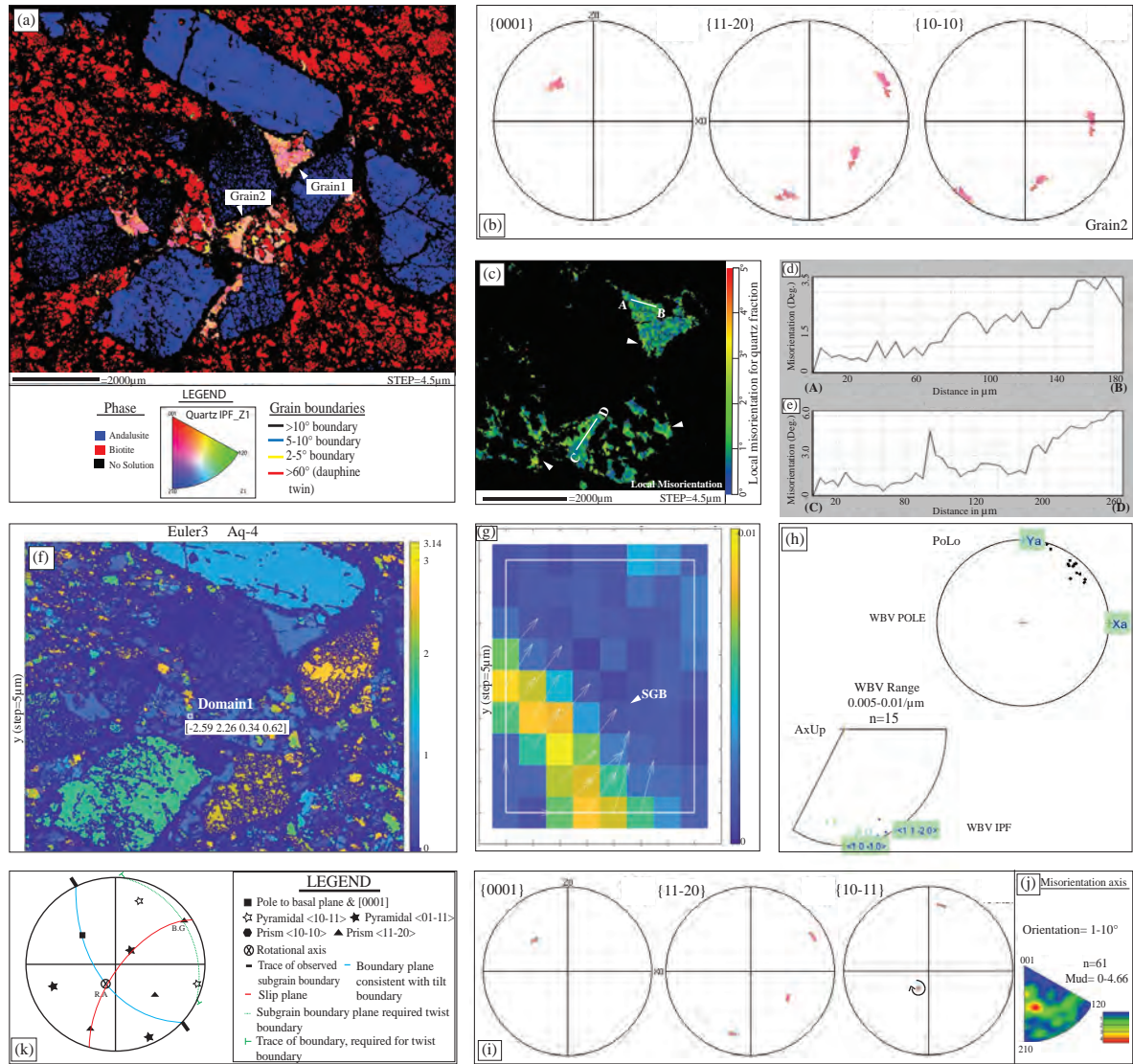
37

Figure 14: a) Map, as shown in figure: 13 e, quartz is outlined by white dashed lines with conventional IPF_Z1 colouring. The step size is 0.5μm. Different grains are marked and domains are shown. 'Domain-1 and 2' are marked for 'Grain6'. b) Legend shows different phase and grain, subgrain boundaries. c) Map as shown in 'figure: 13j' with quartz in dashed lines, 'Domain3' is marked on it. Same colour coding has been maintained as shown in 'b'. d) WBV colour-coded magnitude map over the whole area, as shown in 'a', with similar domains marked on it. e) Pole figure (stereographic, upper hemisphere) shows the misorientation axis (arrowed). f) Inverse pole figure showing points for same data set as in 'e'. g) The 3D WBV is projected ,onto the map of 'd' for 'Domain1', and WBVs> 0.011/μm marked as arrows. The higher magnitude deciphers a subgrain boundary with a similar morphology as shown in 'a'. h) Pole figure, for the same data set of 'Domain1' as shown in 'd' and 'g'. i) IPF for the same data set. Note the clustering of the WBVs along the basal plane at two corners. j-m) Analysis for 'Domain2'. j) Pole figure (stereographic, upper hemisphere) for 'Domain2' with misorientation axis (arrowed). k) The 3D WBV is projected , onto the map of 'd' for 'Domain2', and marked with arrows for >0.004/μm. l) IPF for the same data set. m) Pole figure (stereographic, upper hemisphere) to show schematically the position of the orientation of different axes and pole to planes for 'Domain2'. The interpreted rotational axis (R.A) and burgers vector direction (B.G) are marked (see text for details). n) WBV colour-coded magnitude map over the whole area, as shown in 'c', with same domain marked on it. o) The 3D WBV is projected, onto the map of 'n' for 'Domain3', and marked with arrows for >0.0021/μm. The WBVs are facing each other.

38

single clustering. This defines a combination of dislocation types, here <c+a> (combination of edge dislocation). A schematic diagram (Fig. 14m) for 'Domain1' shows a tilt boundary model for the subgrain boundary plane consistent with a prism plane {11-20}. A slip system can be inferred as (0001) <10-10>, with edge dislocations lying in the prism plane (Tab. 5). Similar analysis for 'Domain1' shows (0001) <01-10> as the developed slip system (Tab. 5). Analysis on the 'Domain3' for 'Grain4' shows higher values of WBVs parallel to the c-axis (Fig. 14n, Tab. 5). And the pole figure shows dispersion for all the axis (not shown here). The projected WBVs for the same data (Fig. 14o) are facing towards each other, similar to Fig. 8j for monzogranite.

Quantitative orientation analysis of subsolidus rock: _Quartz crystallizing from an aqueous fluid in a hornfels:_

The quartz grains are displayed with IPF_Z1 colouring (step size of 4.5 μm) and different grains are marked (Fig. 15a). The 2° subgrain boundaries and dauphine twins are seen to be populated close to the grain edges (Fig. 15a). Since the biotite grains are visibly dispersed, no CPO analysis have been performed. A pole figure dispersion of lattice orientation shows a single dispersion for all the axes (Fig. 15b). The local misorientation map (Fig. 15c) shows a crystal bending along the grain edges (marked with arrows). Misorientation along profiles 'AB' and 'CD' show change in crystal orientation, which goes up to 4-6° (Fig. 15d, e). The WBV magnitude map for 'Domain 1' shows higher WBV values parallel to the 'a1' and 'a2' axis (Fig. 15f, Tab. 5), and reads misorientation in the order of 3.67° (Tab. 5). The projected 3D WBVs mark out a diagonal subgrain boundary trace having long WBVs (Fig. 15g), and a clustering for the same data set can be observed (Fig. 15h). A pole figure dispersion for the same domain shows one of the <10-11> axes as the rotational axis (Fig. 15i). Also, the EBSD inverse pole figure (IPF) shows the same (Fig. 15j). A schematic diagram (Fig. 15k) with all the crystallographic axis shows a tilt boundary model for the subgrain boundary plane is consistent. A subgrain boundary plane as one of the prism planes is found. Additionally, the burgers vector marks the direction of <11-20>, which is fairly consistent (Fig. 15h). The misorientation axis can be explained by a (01-11) <11-20> slip system with edge dislocations lying in the prism plane.

Figure 15: EBSD analysis on rocks from a hornfels : AQ-4 with a step size of 4.5µm for detailed analysis. a) Quartz grains are shown with IPF_Z1 colour coding. 2°, 5° and 10° boundaries are plotted. Andalusite and biotite phases are given a particular phase colour as shown in legend. Different grains are marked. b) 'Grain2' shows atleast a single small scale dispersion in the pole figure. c) Local mis--orientation map is displayed, and higher degree of misorientation is observed at the grain edges. d-e) Change in crystal orientation can be seen along profiles 'AB' and 'CD'. Misorientation goes up to 6-7°. f) WBV magnitude map shows magnitude of weighted burgers vectors. A domain is chosen for subsequent analysis. g) A diagonal trace of subgrain boundary plane can be seen in the 3D WBV figure with all the WBVs> 0.005/µm are shown with a direction. h) Pole figure and IPF for the same data set, as in 'g', shows strong clustering. i) Pole figure (stereographic, upper hemisphere) for this subgrainboundary plane is shown. <10-11> idenifies the rotational axis (marked by an arrow). j) Contoured inverse pole figure (IPF) shows rotational axis for the same data set as in 'i'. k) Pole figure (stereographic, upper hemisphere) to show schematically the position of the orientation of different axes and pole to planes for 'Domain1'.The dispersion of the data is not shown although the interpreted rotational axis (R.A) and burgers vector direction (B.G) are marked (see text for details).

40

Chapter 5: Discussion

5.1. General microstructures indicative of the former presence of melt: Can they be used to distinguish between variable differential stress and/or crystallization-cooling rate environments?

In this study all rocks, except the hornfels, were expected to show optical features typical for the former presence of melt, and have indeed retained a selection of these microstructures (Fig. 2, 3, 4, Tab. 1); they include a. low dihedral angles (LDA) between one grain of the crystallizing phase and two grains from other phase(s) (Fig. 2d, 3c, 3h, 4e-f), b. crystallized interstitial phase exhibiting xenomorphic shape (Fig. 2c, 3e, 3h, 4e), c. melt pockets pseudomorphed by grains with well-developed crystal faces of a single mineral phase (Fig. 2d, 3b, 3h-i) or polycrystalline intergrowths of quartz- plagioclase- K-feldspar (Fig. 4g), typical for felsic melt crystallization (nanogranitoids (e.g. Cesare et al. 2009)). Depending on the volumes of the pore spaces the crystallizing phase(s) either develop aggregates (large volume) or crystallized only as a single mineral phase with blocky outline (small volume), d. the last crystallizing phase in the interstices exhibits cuspate boundaries, or forms sharp pointed extensions (Fig. 2e, 3d, 3g, 4f), e. spatially distributed grains in 2D have similar crystal orientation (deciphered by EBSD orientation map or accessory gypsum plate), forming well-preserved connected 3D melt pockets (Fig. 2e, 3d and Stuart et al., 2018 identifies for Fig. 4e plagioclase grains), f. corroded boundaries of reactant minerals and numerous melt inclusions for partially molten rocks under static and dynamic conditions (Fig. 3b, c, g), g. lack of intense undulose extinction, subgrain formation, and deformation twinning (Fig. 2c, f; 3b, c; 4b, d). Though minor crystal lattice bending identified by moderate undulose extinction can be observed in the monzogranite (Fig. 2c).

Despite these common features, the overall geometric arrangement of these microstructural features distinguishes between samples that have crystallized from melt in static versus dynamic environments. Different to the dynamic cases, the statically crystallized monzogranite and static migmatite a. show quartz-feldspar(s) interfaces with commonly euhedral shape retained by feldspars, b. crystallized quartz as the interstitial melt phase having a low dihedral angle relationship with the surrounding phases, c. lack pervasive or local foliation (e.g. aligned biotite), and d. do not show movement of grain boundaries of a single grain into the surrounding grains (Fig. 2, 3 and Chapter: 4). On the other hand features exclusive to the dynamic environment (dynamic migmatite and melt fluxed shear zone) include a. foliation made by the alignment of an elongate phase such as biotite or amphibole, b. characteristic melt microstructures found only at higher magnification (one

order of magnitude smaller than in the static case) and these are not ubiquitous at the thin section scale, c. preferential orientation (at an angle with the shear plane or parallel to foliation) of very thin former crystallized melt phase along grain boundaries (Fig. 3g-i, 4e), d. post-tectonic melt dykelets pseudomorphing small-scale melt-filled fractures (i.e micro-dykes, figure: 4h, i), and aided by brittle fracturing associated with overpressure of melt migration once the melt crystallizes in the high strain domain (Rybacki et al., 2008; Weinberg and Regenauer-Lieb, 2010; Stuart et al., 2018).

In contrast, when examining all the different samples in terms of inferred crystallization rate, no substantial differences are observed, i.e. between the general microstructures of the granite/ static migmatite (slow crystallization) and the contact aureole dynamic migmatite (faster crystallization under active differential stress). There is no distinct difference in the size distribution of former melt phases or their shape or arrangement.

5.2. Common structures internal to quartz grains pseudomorphing former melt: Are they distinct from structures developed during solid state deformation?

In terms of internal grain microstructures as identified by EBSD and WBV analysis, all the samples show change in crystal orientation within a single grain of quartz (Fig. 6g, h, Fig. 9 f, g, Fig. 11g-i, Fig. 13f, g, k; Tab. 4), and bending at grain edges (Fig. 6i, j, k, Fig. 9h, i, Fig. 11f, Fig. 13h, i). They show, a high population of 2° subgrain boundaries and dauphine twins near to the quartz-neighbour edges (Fig. 6e, f; Fig. 9e; Fig. 11e; Fig. 13e, j). The existence of low angle subgrain boundaries is supported by the disparity between correlated and uncorrelated data set in the misorientation angle distribution profile (Wheeler et al., 2001; Fig. 6l; Fig. 9j; Fig. 11j; Fig. 13n). The grains develop one or two way lattice dispersion without a clear rotational axis (Fig. 6m, n, o; Fig. 9k, l; Fig. 13p, q). This is very different to a solid-state deformation, where the microstructures are organized and the dominant external active stress field results in clear dispersion patterns at the grain scale. No strain induced preferred orientation of the crystal lattice (CPO) can be seen for all the array of rocks (Fig. 6b, d, Fig. 9b, d), even under the dynamic condition (Fig. 11b, d, Fig. 13b, d and Stuart et al., 2018). The general lack of CPO even when differential stress was prevalent suggests quartz/feldspars grains do not take up strain during crystallization, different to the solid state deformation. This is particularly interesting in the case of the dynamic migmatite and the melt-fluxed shear zone. The absence of CPO in a deformed rock can also be correlated with the diffusion creep instead of intracrystalline plasticity and can be controlled

by diffusion or frictional grain boundary sliding (GBS) (Law, 1990, Prior et al., 1999). But the retention of magmatic features at the optical scale clearly indicate absence of any diffusion creep. There is also no systematic lattice reorientation and/or systematic grain rotation as seen during solid state deformation in the dislocation creep regime (Drury and Urai, 1990; Hirth and Tullis, 1992 etc., Tab. 2). Hence, once the melt phase solidifies the deformation must have taken up in the vicinity, either in areas where melt is still present or in rheologically weaker areas (see also Pakrash et al. 2018). Lack of post-crystallization solid state overprinting features suggest that the rocks once solidified are very resistant to deformation – a feature similar to reaction hardening (Wintsch and Yeh, 1999). This could be due to a strong network of grains pseudomorphing the melt networks.

5.3. Structures internal to quartz grains pseudomorphing former melt: Can they be used to distinguish between differential stress and/ or crystallization-cooling rate environments?

There are systematic small scale differences when the slowly cooled interstitial melt pseudomorphs (like monzogranite/ static migmatite) are compared with the dynamically (syntectonic) fast cooled melt phases. The fast-cooled varieties mostly show smaller changes in crystal orientation and bending, in the order of 2.5-4° (Fig. 11i, Fig. 13f, g, k; Tab. 4; Chapter: 4). In contrast, the slowly-cooled rocks show a change in the order of 4-6° (Fig. 6g, h, Fig. 9f, g; Tab. 4; Chapter: 4) in monzogranite or static migmatite. Associated lower order misorientations are also observed in WBVs analysis (Chapter: 4; Tab. 5). The amount of pole figure dispersion is also found to be higher for slowly-cooled varieties compared to the fast-cooled melt in the shear zone (Chapter: 4; Tab. 4). A higher degree of pronounced crystal bending is also seen for monzogranite and static migmatite (Fig. 6i-j, Fig. 9h-i; Chapter: 4). The higher internal misorientation associated with slow crystallization is also seen in the lower stress variant sample (quartz grains in the dykelet, PV1208-2) adjacent to the melt fluxed shear zone (Fig. 13m, Tab. 4), which shows an internal orientation change in the order of 4-6°. This is very similar to observation made in monzogranite. They also show higher order crystal bending at the grain edges in the order of 4-5° (Fig. 13o), and hence act as a proxy to the monzogranite (due to the similar environment of origin).

A difference between the dynamic migmatite and other samples is the high internal grain misorientation seen across the whole quartz fraction (Fig. 11j; Chapter: 4). There is a high frequency of low angles observed in the misorientation distribution in dynamic migmatite (Fig. 11j), and is interpreted to be due to the fact that in such a bulk analysis, a

certain fraction of the data is derived from protolith quartz grains with a subsolidus deformation history. When looked into detail (e.g. Grain 1; Tab. 4, Fig. 11e, g, h), internal misorientation reaches 9°, but continuous lattice bending is absent. Misorientations are concentrated at low angle boundaries which are dominantly around 2-3° but higher angle boundaries of 5° also occur. Importantly the high internal misorientation and dauphine twins are observed throughout the whole grain, in contrast to misorientations concentrated at the grain edges/ two grain contacts for the fast and slowly cooled, static rocks.

5.4 Dislocation types and slip systems activation in quartz crystallized from a melt: Comparison with slip system activation induced by crystal-plastic deformation at subsolidus conditions

Solid state crystal plastic deformation of quartz results in the development of CPO the character of which is controlled by the activation of particular slip systems. The activation of a slip system depends on whether the critical resolved shear stress can be overcome. As the critical resolved shear stress is different for different slip systems at different boundary conditions, the activation of a slip system or slip system combination is dependent on temperature, strain rate, differential stress and fluid content (e.g. Law, 2014). In general, at low temperatures, dislocation slip and glide becomes important on the basal glide plane with the development of (c) <a> slip system (Tab. 6, Passchier and Trouw, 2005), while at higher temperatures a transition from prism <a> slip to prism <c> slip is activated (e.g. Tab. 6, Passchier and Trouw, 2005). At high temperatures, there is still ongoing discussion about slip system activation. Okudaira et al. (1995) demonstrated petrologically that the transition temperature from basal <a> to prism [c] slip system occurs at around 550-660°C with natural strain rates in high temperature metamorphic tectonites. Numerous others slip system have also been observed (Bäeta and Ashbee, 1969), including slip on the prism planes 'm' parallel to 'c+a' (between 700-850°C), and on second-order pyramidal planes {2111} parallel to 'c+a' (at temperature >750°C). Dauphine deformation twins are described at low grade conditions as well as in high grade rocks (e.g. Tullis, 1970; Llyod et al., 2004). The existence of well-developed subgrain walls is generally attributed to dislocation generation and rearrangement during crystal plastic deformation and syn- or post tectonic recovery (Wilsdorf and Hansen, 1991; Hirth and Tullis, 1992; Borthwick and Piazolo, 2010). Only recently it has been recognized that during fluid mediated replacement reactions, subgrain walls can also be developed, but they are less well defined in terms of common dislocation type (Spruzeniece et al. 2016). Evidence of systematic dislocation

generation related to dislocation glide or climb can be seen from the single or double small circle dispersions of the crystal lattice orientation for individual quartz grains shown on pole figures (e.g. Reddy et al. 2007). If these dispersions are well defined and the rotational axis can be deciphered, they can be related to slip systems (see Chapter: 2; e.g. Reddy et al. 2007, Piazolo and Jaconelli, 2014). While for some grains in the analysed samples single and double dispersion paths are readily observed (e.g. Fig. 6n, o, Fig. 9k, l, Fig. 13q), and for many grains the lattice dispersions are poorly defined (e.g. Fig. 6m, Fig. 13p). In both cases determining the rotational axis (having least change in lattice dispersion in the pole figure) is very difficult, since all the axes either do not show substantial dispersions or grains may show dispersions for all the crystallographic axes. It means either a non-systematic slip system has been generated (like in replacement reactions), or a mixture of slip systems have caused the dispersion for all crystallographic axes. Also, overlapping of dauphine twins on top of each other in the pole figure makes it more unorganized. The small angle misorientation axis, analysed for a single grain, also lack any preferential development of a single rotation axis (Fig. 7c). This could be due to the development of a mixture of slip systems or an error associated with small angle measurements (Wheeler et al., 2001). Also, the exact slip systems based on CPO figures cannot be translated as all the representative samples do not show any preferential orientation. Hence analysis on subgrain boundaries are found to be crucial. In the undeformed slowly cooled monzogranite and even within a single grain an array of representative slip systems are identified (refer to Chapter: 4, Tab. 5 and Tab. 6). The observed (0001) <11-20> slip system would infer a conventional lower temperature and higher strain rate response (Tab. 5), and the {10-10} <2-1-10> slip system would be expected to develop at higher temperatures and lower strain rate (Tab. 5), whereas the {10-10} [0001] has been shown to be only activated at temperatures above 700°C. Activation of all these slip systems within one single grain has not been reported from subsolidus deformation. According to Paterson et al., 1989, when prism [c] slip is associated with igneous intrusions, it should indicate deformation near the granitic solidus, which is not the case here. Apart from this, a combination of edge dislocations <c+a> are also seen (Tab. 5). The monzongranite also shows development of subgrain walls parallel to both the basal plane (Fig. 7k), and prism plane (Fig. 7q, 8q) which is conventionally described as high temperature deformation of quartz (> 650°C) or 'chessboard extinction' (Tubia and Cuevas, 1986; Blumenfeld et al., 1986; Okudaira et al., 1995; Kruhl, 1996). All these represent a disagreement of activation of these slip systems with the temperature range required under subsolidus condition, and also cannot be linked with the outside stress regime

(since there is no CPO). This denotes a distinct mode of genesis different from the typical solid state deformation in mylonites. Apart from the dislocations associated with subgrain boundaries little distortion is seen within the grain (Tab. 5 'Domain6', Fig. 8o). This suggests that recovery plays a minor role in formation of the subgrain boundaries. Also the morphology of these boundaries are rugged, not straight as one might expect for normal recovery subgrains. In the static migmatite a similar set of slip systems are activated, both corresponding to conventional lower temperature ((0001) <10-10>) and higher temperature ({11-20} <0001>) conditions (Tab. 5/6). In addition, slip on the pyramidal/ rhomb plane parallel to one of the a-axis {01-11} <10-10> and the presence of 'c+a' edge dislocations are observed (Tab. 5). Interestingly, even within the melt fluxed shear zone the general spread in slip systems activated is similar. Both basal <a>, and prism [c] (not shown here) are seen with a dominance of edge dislocations (Fig. 6, Tab. 5/6). In the dynamic (syntectonic) migmatite activation of high temperature prism and rhomb slip planes are also found to be true (Tab. 5/6) with slip directions parallel to <a> and rhomb direction <r>.

Table: 6 *Comparison of conventional quartz slip systems as described for a mylonitic rock deformed under subsolidus condition (from Law, 2014 and references therein) with the slip systems as observed for the array of melt bearing rocks under static and dynamic condition.*

Conventional slip systems for solid-state deformation at various strain rate and temperature					
Rocks	*Slip system(s)*	*Slip plane(s)*	*Slip direction*	*Strain rate*	*Temperature*
Subsolidus sheared rock	*(0001)<-1-120>*	*Basal (c)*	*<a>*	*High ($10^{-13}s^{-1}$)*	*280-400°C*
	{10-10}<-1-120> {1101}<-1120>	*Prism {m} Rhomb {r/z}*	*<a>*	*Lower ($<10^{-13}s^{-1}$)*	*400-650°C*
	{10-10} [0001]	*Prism {m}*	*[c]*	*Lower ($<10^{-13}s^{-1}$)*	*650-700°C*
Observed slip systems for the array of melt bearing rocks					
Granite	*{10-10} [0001] (0001) <11-20> {11-20} [0001]*	*On all planes*	*In all possible directions: <a>, [c] and <a+c>*	*Zero*	*~650-900°C*
Static migmatite				*Zero*	*~800°C*
Melt fluxed shear zone	*{10-10}<2-1-10> {01-11} <10-10>*	*Basal (c) Prism {m} Rhomb {r/z}*		*High * in bulk rock*	*~650-850°C*
Aqueous	*(0001) <01-10>*			*Zero*	*~400-450°C*
Dynamic migmatite	*{01-11} <01-11> {11-20} <10-11>*	*Rhomb {r/z} Prism {m}*	*<a>, <r>*	*High * in bulk rock*	*~660°C*
	{10-11} [0001]	*Rhomb {r/z}*	*[c]*		

In summary, a quartz grain crystallized from melt shows consistently a mix of edge dislocation types (<a>, [c] and <a+c>), and activation of several slip systems inconsistent with the commonly-described subsolidus microstructure of quartz in a mylonite (Fig. 6). Hence, all these high temperature felsic melt present rocks show dislocations related to both

the basal plane (commonly, the low temperature slip plane, Tab. 6) and basal direction (as high temperature slip direction) forming the lower and upper bounds of possible slip systems (Tab. 6).

In the presented data set, the difference in slip system activation characteristics is well illustrated by the discrepancy in internal deformation features of melt crystallized grains and the grains that are interpreted to have deformed pre-melting in a solid state (e.g. Grain 1 of the WJ1650 sample, Fig. 11e) in the dynamic migmatite. This grain shows only edge dislocations parallel to <a> with development of {11-20} <10-11>, or {01-11} <01-11> and {11-20} <11-20> slip systems, but no activation of basal slip plane or direction parallel to c-axis is observed (Tab. 5). Slip only on the rhomb or prism plane, with <a> as slip direction, can be coined as high temperature subsolidus deformation (Tab. 6). Hence, only a single type of high-T slip system with only a single edge dislocation type has been activated; this further supports the interpretation that this grain represents a quartz grain that underwent subsolidus deformation in a high-T shear zone. Hence, there is a substantial difference in the types of generated slip systems associated with a single quartz grain when it undergoes solid state deformation as opposed to a crystallizing phase at interstices.

5.5 Differences and similarities between growth from a silicate melt versus growth from an aqueous fluid

Since features associated with crystallizing interstitial melt phases are seen to be consistent for all the array of rocks (with or without active external stress) and are rather related to the internal strain (due to the variable local built up of stress), this process should also act similarly for the interstitial quartz grain crystallized from an aqueous fluid. Here, indeed a two-way dispersion for the crystallographic axis is observed (Fig. 15b), with no particular development of a rotational axis, similar to the melt-present rocks. Individual grains also show crystal bending at the grain edges (Fig. 15c) and a change in the crystal orientation in the order of 3–6° (Fig. 15d, e). The higher values of misorientation indicates its similarities with the slowly crystallizing quartz phase in monzogranite and static migmatite (compared to dynamic ones), and is also corroborated by the absence of any external active stress acting on them.

The mineral associations of biotite + andalusite in this sample shows a temperature range of 400–450°C. A prism slip plane with <a> crystallographic direction would be expected for a similar temperature range for quartz (Tab. 6), if developed under solid state deformation. However, generation of mixed nature of dislocations (two types of edge) with

an inconsistency in the slip plane (with activation of rhomb plane as opposed to prism plane) e.g (01-11) <11-20>, mimics its microstructural similarity with quartz pseudomorphing melt pockets as we have seen before (Tab. 6). This also justifies that these features are intrinsic properties of a crystallizing phase at the interstices irrespective of whether the quartz is crystallizing from a melt or an aqueous fluid, and is substantially different from a quartz deformed under solid state.

5.6 Origin of internal lattice distortion in interstitial phases crystallizing from a melt

For grains pseudomorphing melt, there is no systematic grain reorientation developing a CPO, even though at the grain scale, the internal lattice distortions are abundant. This suggests that a local build-up of stress must have prevailed during the interstitial phase growth, while no long-range stress was dominating. This is supported by the observed change in crystal orientation within individual grains, the presence of numerous subgrain boundaries, crystal bending along the quartz-neighbour edges/ or two grain contacts, misorientation angle distributions with a high abundance of low angles and abundant dauphine twins. Let us consider the processes and stress conditions when a melt crystallizes in a confined porous space. There is very little in-depth work on crystallization of a melt/ aqueous fluid in pore spaces in the geosciences (see McNamara et al., 2016). However, the growth of minerals in confined environments occurs in many places of the Earth including vein initiation and growth (Fletcher and Merino, 2001), salt growth in pore spaces (Wellman and Wilson, 1965; Scherer 2004 etc.), and mineral growth in the injection wall due to CO_2 sequestration (Muller et al., 2009). During crystallization from a supersaturated fluid mechanical forces may be exerted. Forces are thought to stem largely from volumetric changes associated with hydration/ oxidation/ mineral replacement (Putnis, 2002; Jamtveit et al. 2009). Three different scenarios can be considered:

1. <u>Force exerted due to the surface energy differences of fluid/solid interface (due to the difference in physical properties):</u> If we consider a large crystal of ice immersed in water at 0°C in a pressure P_l, it would have no tendency to grow. However, if the temperature decreases the ice will start to grow simply due to the change in chemical potential (free energy per mole) at the ice-water interface. The crystal experiences compressive stress as a result of its surface energy (Υ_{cl}), and due to the crystal/liquid curvature K_{cl}. The capillary pressure inside the crystal (P_c) is given by Laplace's equation (Scherer, 1993; Defay and Prigogine, 1966):

$$P_c = \frac{p_l + \Upsilon_{cl}\kappa_{cl}}{}$$

The capillary force is a function of the curvature of the interface between solid and liquid, and exerts compressive forces on the crystal if Kcl >0.

Now if a crystal, with a surface energy of Υ_{cs}, enters in a cylindrical pore with a radius r_p having a contact angle between the crystal and the pore wall of Θ, then the capillary pressure in the crystal is:

$$p_c = p_l - \frac{2\gamma_{cl}\cos(\theta)}{r_p}$$

And the radial stress on the pore wall:

$$\sigma_r = \frac{\gamma_{cs} + 2\gamma_{cl}\cos(\theta)}{r_p} - p_l$$

However, when the contact angle exceeds 90°, there is a hoop tension in the pore walls; and the pore wall will exert a stress on the crystal to suppress its growth in the radial direction (Scherer, 1999). If the contact angle is less, then the generated stress is low, when Θ <90° the crystallization could generate compressive stress in the body. Since for most of the granitic system the wetting angle is <60°, a compressive stress can build up. This might increase when the melt is crystallizing slowly with increasing surface contact of growing phase and pore boundaries. Hence more dislocations are seen in the rim of the growing grains of granite or static migmatite.

2. <u>Force of crystallization</u>: Stresses may develop due to mineral crystallization in confinement and can be described as:

$$\nabla P = \frac{RT}{V_s}\ln(S)$$

Where R is the molar gas constant, V_s is the molar volume of the solid phase (e.g. salt), T is the temperature, and S denotes degree of supersaturation. ∇P is often referred to as "force of crystallization" (Wellman and Wilson, 1965; Scherer 2004).

There could also be van der Waals forces when two different solids are separated by a liquid (Ninham and Parsegian, 1970). In a confined region non uniform stress is observed by Càmara and Bresme, 2003, and the major changes are only associated with the pore edges. All these models describe a local stress generated at the pore wall and exerted by a crystallizing phase, when crystallizing as an interstitial pore. This local stress depends on the degree of supersaturation and the difference in chemical potential between the solid and liquid phase. And should be much higher in the case of magma compared to water, due to its higher viscosity.

3. <u>Volumetric change inducing localized forces:</u> Forces are thought to stem largely from volumetric changes associated with hydration/ oxidation/ mineral replacement (Putnis, 2010; Jamtveit et al. 2009). Volume expansion associated with local metamorphic reactions are demonstrated in a variety of geological settings and ranges from granulite facies migmatites to serpentinization (Watt et al., 2000; Jamtveit et al., 2009). Ostapenko, 1976 describes 'swelling pressure' related to oxidation reactions, and can reach 10-100 MPa, depending on the strain rate. Experimental studies have also shown local fracturing caused by the melting reaction (Connolly et al., 1997). All these examples represent a local development of elastic stresses without a major deviatoric stress field outside, very similar to what is observed here.

In the studied rocks which have crystallized at moderate confining pressure (~ 2 to 4 kbar; monzogranite, static migmatite), and at elevated confining pressure (~11kbar; melt fluxed shear zone), the local stress at the grain boundary of a crystallizing quartz grain must have caused the internal deformation seen. If we consider the whole system is under a confined pressure of P_{con}, the outward pore pressure of the crystallizing phase is ∇P, and this developed due to the force of crystallization (as discussed in 'scenario 2'). A local deviatoric stress is expected to develop because of the existence of two opposite and unequal forces. This would act on the boundary wall separating these two phases. The stress will be equal to (P_{con} -∇P). However, the effect of capillary pressure (P_c) on the crystallizing phase is compressional too (as discussed in 'scenario 1'), and hence will add to the confining pressure component P_{con}. Interestingly, the effect of this locally derived stress on the microstructure of quartz, crystallizing in a confined space, is seemingly less during fast crystallization and higher confining pressure. If we equate the degree of internal deformation i.e. dislocation density to degree of stress assuming that dislocation density is proportional to differential stress (after Bailey and Hirsch, 1960), then it must be concluded that a system that solidifies quickly and exhibits low crystal misorientations/bending must have experience lower effective stresses than a slowly cooled felsic melt pocket which shows higher dislocation densities. The fast crystallization may inhibit higher stress built up since the system solidifies quickly, and the local deviatoric stress terminates as soon as the last droplet of melt solidifies. Another explanation involves the effect of high confining pressure when P_{con} >>∇P, and thus a lesser pronounced effect of pore pressure is seen. However, a locally derived grain scale pore pressure at the boundary of a crystallizing quartz grain (from melt/aqueous) is seen to have an effect on the evolution of its microstructure producing all

possible slip systems and a combination of edge dislocations, and this is characterised mainly by the change in crystal orientation, 'bottleneck' crystal bending and low angle (<5°) subgrain boundaries. A high population of dauphine twins at the grain edges indicate an increase in the stress level with closure of the pore space. Since the whole system starts at higher temperature, the slip systems corresponding to that temperature can initiate, and as the system starts to cool lower temperature slip systems start to be activated. This might have caused the activation of all slip planes and directions in the quartz grains. Thus in the slowly cooled monzogranite both the basal and prism subgrain boundaries are seen, and explains the existence of chessboard pattern without the prevalence of any external active stress.

6: Conclusions

The present study describes all the general optical microstructures of quartz grains solidifying in a strain free granitic system as opposed to a crystallized interstitial melt phase in a shear zone. They are found to be different, but also have several similar features when studied in detail. This is also true for partially molten rocks, under static and dynamic conditions. Though they have many differences and similarities in the optical scale, a list of similar conspicuous features are identified at the micron scale employing EBSD analysis. The present study reveals for the first time that interstitial quartz grown from a melt or aqueous fluid phase can exhibit crystal bending and subgrain boundary development without developing CPO at thin section scale. This is irrespective of quartz grains crystallizing in interstices from an aqueous fluid or melt, and also does not correspond to the external stress field. The development of crystal bending, changes in crystal orientation, dispersion in pole figures, and a higher population of subgrain boundaries along crystal edges all suggest minor stress concentrations, active at the crystallizing grain edges caused these deformation features. However, very subtle changes in the general responses of crystallizing quartz under static or dynamic condition are also found to be related to the crystallization rate and/or confining pressures. Activation of several slip systems are seen to persist within a single rock, even when a single grain is analysed. They correspond to a wide range of temperature e.g. <650°C (by developing <a> slip on basal, prism, and rhomb planes), >650°C (with active <c> slip) and even >750°C (<c+a> slip). The generation of different slip systems without activation of any CPO differentiates melt pseudomorphed quartz from quartz that was deformed under subsolidus conditions. Until now, the development of substructures characterized by dislocations associated with several slip systems of quartz (depending on

temperature) were only described in response to subsolidus crystal plastic deformation induced by differential stress conditions. But here it is demonstrated that they are also present in quartz grains on which the effect of external active stress is almost zero (*static*). This provides us with a tool box to identify them in comparison to a grain that underwent solid state subsolidus deformation.

Future work directions:

      This study represents an exploratory study on the crystallization of interstitial fluids and their characteristics. The next step of research should focus in detail at the plausible reason(s) for the development of local crystallization stresses. The following steps could be taken to enable further insight. 1) Further study of the observed relative population of subgrain boundaries and crystal bending being higher in the case of quartz, but less for plagioclase that has crystallized in its vicinity (not presented here). This is true for all rocks studied. Also, the number of grains having a higher misorientation is more in quartz compared to its feldspar counterpart. This may be due to the fact that plagioclase with higher anorthite content is the initial phase to be crystallized according to the Bowen's reaction series in a crystallizing felsic melt, and hence could exert pressure on the growing crystal of quartz at its vicinity. However, to successfully verify this first interpretation, a study of e.g. gabbro samples could be undertaken. This will help to understand the influence (if there is any) of one phase onto the other in the evolution of these microstructures. 2) Experiments with quartz grown out of silicate melt/ aqueous fluid phase can also be used to verify the observations when performed at different confining pressures. 3) Numerical simulations allowing the three scenarios for stress concentration development listed in the discussion to be tested would enable insights into the underlying causal relationships. At the same time, such models may help to explain in detail the observed loci of stress concentrations.

7: References

Allibone, A.H., Jongens, R., Scott, J.M., Tulloch, A.J., Turnbull, I.M., Cooper, A.F., Powell, N.G., Ladley, E.B., King, R.P. and Rattenbury, M.S., 2009. Plutonic rocks of the Median Batholith in eastern and central Fiordland, New Zealand: field relations, geochemistry, correlation, and nomenclature. *New Zealand Journal of Geology and Geophysics*, *52*(2), pp.101-14

Ashworth, J.R., 1972. *Migmatites of the Huntley-Portsoy area, North-East Scotland* (Doctoral dissertation, University of Cambridge).

Ashworth, J.R., 1976. Petrogenesis of migmatites in the Huntly-Portsoy area, North-east Scotland. *Mineralogical Magazine*, *40*(315), pp.661-682.

Ashworth, J.R., 1979. Comparative petrography of deformed and undeformed migmatites from the Grampian Highlands of Scotland. *Geological Magazine*, *116*(6), pp.445-456.

Bachmann, O. and Bergantz, G.W., 2004. On the origin of crystal-poor rhyolites: extracted from batholithic crystal mushes. *Journal of Petrology*, *45*(8), pp.1565-1582.

Baëta, R.D. and Ashbee, K.H.G., 1969. Slip systems in quartz: I. Experiments. *American Mineralogist: Journal of Earth and Planetary Materials*, *54*(11-12), pp.1551-1573.

Bailey, J.E. and Hirsch, P.B., 1960. The dislocation distribution, flow stress, and stored energy in cold-worked polycrystalline silver. *Philosophical Magazine*, *5*(53), pp.485-497.

Bestmann, M. and Prior, D.J., 2003. Intragranular dynamic recrystallization in naturally deformed calcite marble: diffusion accommodated grain boundary sliding as a result of subgrain rotation recrystallization. *Journal of Structural Geology*, *25*(10), pp.1597-1613.

Binns, R.A., 1966. Granitic intrusions and regional metamorphic rocks of Permian age from the Wongwibinda district, northeastern New South Wales. In *Journal and Proceedings of the Royal Society of New South Wales* (Vol. 99, pp. 5-36).

Blumenfeld, P., Mainprice, D. and Bouchez, J.L., 1986. C-slip in quartz from subsolidus deformed granite. *Tectonophysics*, *127*(1-2), pp.97-115.

Borthwick, V.E. and Piazolo, S., 2010. Post-deformational annealing at the subgrain scale: Temperature dependent behaviour revealed by in-situ heating experiments on deformed single crystal halite. *Journal of structural geology*, *32*(7), pp.982-996.

Brown, M., 1973. The definition of metatexis, diatexis and migmatite. *Proceedings of the Geologists' Association*, *84*, pp.371-IN2.

Brown, M. and Solar, G.S., 1999. The mechanism of ascent and emplacement of granite magma during transpression: a syntectonic granite paradigm. *Tectonophysics*, *312*(1), pp.1-33.

Brown, M. and Rushmer, T. eds., 2006. *Evolution and differentiation of the continental crust*. Cambridge University Press.

Brown, M., 2010. Melting of the continental crust during orogenesis: the thermal, rheological, and compositional consequences of melt transport from lower to upper continental crust. *Canadian Journal of Earth Sciences*, *47*(5), pp.655-694.

Cámara, L.G. and Bresme, F., 2003. Molecular dynamics simulations of crystallization under confinement at triple point conditions. *The Journal of chemical physics*, *119*(5), pp.2792-2800.

Cesare, B., Ferrero, S., Salvioli-Mariani, E., Pedron, D. and Cavallo, A., 2009. "Nanogranite" and glassy inclusions: The anatectic melt in migmatites and granulites. *Geology*, *37*(7), pp.627-630

Clemens, J.D., 1998. Observations on the origins and ascent mechanisms of granitic magmas. *Journal of the Geological Society*, *155*(5), pp.843-851.

Clemens, J.D. and Holness, M.B., 2000. Textural evolution and partial melting of arkose in a contact aureole: a case study and implications. *Visual Geosciences*, *5*(4), pp.1-14.

Clemens JD, Buick IS, Kisters AFM (2017a) The Donkerhuk batholith, Namibia: a giant S-type granite emplaced in the mid crust,
in a fore-arc setting. J Geol Soc Lond 174:pp.157–169.

Clemens JD, Buick IA, Kisters A, Frei D (2017b) Petrogenesis of the Donkerhuk batholith in the Damara Belt of Namibia: protracted, syntectonic, short-range magma transfer in the mid-crust. *Contrib Mineral Petrol, 172*, pp.50.

Cmíral, M., Gerald, J.D.F., Faul, U.H. and Green, D.H., 1998. A close look at dihedral angles and melt geometry in olivine-basalt aggregates: a TEM study. *Contributions to Mineralogy and Petrology*, *130*(3-4), pp.336-345.

Coleman, D.S., Gray, W. and Glazner, A.F., 2004. Rethinking the emplacement and evolution of zoned plutons: Geochronologic evidence for incremental assembly of the Tuolumne Intrusive Suite, California. *Geology*, *32*(5), pp.433-436.

Coleman, D.S., Bartley, J.M., Glazner, A.F., Law, R.D., 2005. Incremental assembly and emplacement of Mesozoic plutons in the Sierra Nevada and White and Inyo Ranges, California. Geological Society of America Field Forum Field Trip Guide (Rethinking the Assembly and Evolution of Plutons: Field Tests and Perspectives, 7–14 October, 2005). doi:10.1130/2005.MCBFYT.FFG

Connolly, J.A.D., Holness, M.B., Rubie, D.C. and Rushmer, T., 1997. Reaction-induced microcracking: an experimental investigation of a mechanism for enhancing anatectic melt extraction. *Geology*, *25*(7), pp.591-594.

Craven, S.J., Daczko, N.R. and Halpin, J.A., 2012. Thermal gradient and timing of high-T–low-P metamorphism in the Wongwibinda Metamorphic Complex, southern New England Orogen, Australia. *Journal of Metamorphic Geology*, *30*(1), pp.3-20.

Debat, P., Soula, J.C., Kubin, L. and Vidal, J.L., 1978. Optical studies of natural deformation microstructures in feldspars (gneiss and pegmatites from Occitania, southern France). *Lithos*, *11*(2).

Dempsey, E.D., Prior, D.J., Mariani, E., Toy, V.G. and Tatham, D.J., 2011. Mica-controlled anisotropy within mid-to-upper crustal mylonites: an EBSD study of mica fabrics in the Alpine Fault Zone, New Zealand. *Geological Society, London, Special Publications*, *360*(1), pp.33-47.

Drury, M.R. and Humphreys, F.J., 1986. The development of microstructure in Al-5% Mg during high temperature deformation. *Acta Metallurgica*, *34*(11), pp.2259-2271.

Drury, M.R. and Urai, J.L., 1990. Deformation-related recrystallization processes. *Tectonophysics*, *172*(3-4), pp.235-253.

Einaudi, M.T., 1977. Petrogenesis of the copper-bearing skarn at the Mason Valley Mine, Yerington District, Nevada. *Economic Geology*, *72*(5), pp.769-795.

Farmer, M., 2018, Migmatite delineates zones of melt flux through the upper crust, Wongwibinda, NSW.

Fazio, E., Punturo, R., Cirrincione, R., Kern, H., Pezzino, A., Wenk, H.R., Goswami, S. and Mamtani, M.A., 2017. Quartz preferred orientation in naturally deformed mylonitic rocks (Montalto shear zone–Italy): a comparison of results by different techniques, their advantages and limitations. *International Journal of Earth Sciences*, *106*(7), pp.2259-2278.

Fletcher, R.C. and Merino, E., 2001. Mineral growth in rocks: kinetic-rheological models of replacement, vein formation, and syntectonic crystallization. *Geochimica et Cosmochimica Acta*, *65*(21), pp.3733-3748.

Gapais, D. and White, S.H., 1982. Ductile shear bands in a naturally deformed quartzite. *Texture, Stress, and Microstructure*, *5*(1), pp.1-17.

Glazner, A.F., Bartley, J.M., Coleman, D.S., Gray, W. and Taylor, R.Z., 2004. Are plutons assembled over millions of years by amalgamation from small magma chambers?.*GSA today*, *14*(4/5), pp.4-12.

Graeter KA, Beane RJ, Deering CD, Gravley D, Bachmann O. , 2015 Formation of rhyolite at the Okataina volcanic complex, New Zealand: new insights from analysis of quartz clusters in plutonic lithics. *Am Mineral, 100*, pp.1778–1789.

Guillope, M. and Poirier, J.P., 1979. Dynamic recrystallization during creep of single-crystalline halite: An experimental study.*Journal of Geophysical Research: Solid Earth*, *84*(B10), pp.5557-5567

Guernina, S. and Sawyer, E.W., 2003. Large-scale melt-depletion in granulite terranes: an example from the Archean Ashuanipi Subprovince of Quebec. *Journal of Metamorphic Geology*, *21*(2), pp.181-201.

Halfpenny, A., Prior, D.J. and Wheeler, J., 2006. Analysis of dynamic recrystallization and nucleation in a quartzite mylonite. *Tectonophysics*, *427*(1-4), pp.3-14.

Hasalová, P., Schulmann, K., Lexa, O., Štípská, P., Hrouda, F., Ulrich, S., Haloda, J. and Týcová, P., 2008a. Origin of migmatites by deformation-enhanced melt infiltration of orthogneiss: A new model based on quantitative microstructural analysis. *Journal of Metamorphic Geology*, *26*(1), pp.29-53.

Hasalová, P., Štípská, P., Powell, R., Schulmann, K., Janoušek, V. and Lexa, O., 2008b. Transforming mylonitic metagranite by open-system interactions during melt flow. *Journal of Metamorphic Geology*, *26*(1), pp.55-80.

Herring C (1951) Some theorems on the free energies of crystal surfaces. *Phys Rev, 82*, pp.87–93.

Hibbard, M.J., 1965. Origin of some alkali-feldspar phenocrysts and their bearing on petrogenesis. *American Journal of Science, 263*, pp.245–261.

Hirth, G. and Tullis, J., 1992. Dislocation creep regimes in quartz aggregates. *Journal of Structural Geology*, *14*(2), pp.145-159.

Hobbs, B.E., 1968. Recrystallization of single crystals of quartz. *Tectonophysics*, *6*(5), pp.353-401.

Hobbs, G.J., 1968. *The geology of the South Shetland Islands: IV. The geology of Livingston Island* (Vol. 47). British Antarctic Survey.

Holness, M.B. and Clemens, J.D., 1999. Partial melting of the Appin Quartzite driven by fracture-controlled H 2 O infiltration in the aureole of the Ballachulish Igneous Complex, Scottish Highlands. *Contributions to Mineralogy and Petrology*, *136*(1-2), pp.154-168.
Holness, M.B., Nielsen, T.F. and Tegner, C., 2006. Textural maturity of cumulates: a record of chamber filling, liquidus assemblage, cooling rate and large-scale convection in mafic layered intrusions. *Journal of Petrology*, *48*(1), pp.141-157.

Holness, M.B., Tegner, C., Nielsen, T.F., Stripp, G. and Morse, S.A., 2007. A textural record of solidification and cooling in the Skaergaard intrusion, East Greenland. *Journal of Petrology*, *48*(12), pp.2359-2377.

Holness, M. B., & Sawyer, E. W., 2008. On the pseudomorphing of melt-filled pores during the crystallization of migmatites. *Journal of Petrology*, *49*(7), 1343-1363.

Holness, M.B., Clemens, J.D. and Vernon, R.H., 2018. How deceptive are microstructures in granitic rocks? Answers from integrated physical theory, phase equilibrium, and direct observations. *Contributions to Mineralogy and Petrology*, *173*(8), p.62.

Holness, M.B., 2018. Melt segregation from silicic crystal mushes: a critical appraisal of possible mechanisms and their microstructural record. *Contributions to Mineralogy and Petrology*, *173*(6), p.48.

Hollis, J.A., Clarke, G.L., Klepeis, K.A., Daczko, N.R. and Ireland, T.R., 2004. The regional significance of Cretaceous magmatism and metamorphism in Fiordland, New Zealand, from U–Pb zircon geochronology. *Journal of Metamorphic Geology*, *22*(7), pp.607-627.

Howell, D., Piazolo, S., Dobson, D.P., Wood, I.G., Jones, A.P., Walte, N., Frost, D.J., Fisher, D. and Griffin, W.L., 2012. Quantitative characterization of plastic deformation of single diamond crystals: A high pressure high temperature (HPHT) experimental deformation study combined with electron backscatter diffraction (EBSD). *Diamond and Related Materials*, *30*, pp.20-30.

Jamtveit, B., Putnis, C.V. and Malthe-Sørenssen, A., 2009. Reaction induced fracturing during replacement processes. *Contributions to Mineralogy and Petrology*, *157*(1), pp.127-133

Jones, K.A. and Brown, M., 1990. High-temperature 'clockwise'P-T paths and melting in the development of regional migmatites: An example from southern Brittany, France. *Journal of Metamorphic Geology*, *8*(5), pp.551-578.

J.P. Poirier, 1985. Creep of Crystals, *Cambridge University Press, Cambridge, pp.260*
Jessell, M.W., 1987. Grain-boundary migration microstructures in a naturally deformed quartzite. *Journal of Structural Geology*, *9*(8), pp.1007-1014.

Kelemen, P.B. and Dick, H.J., 1995. Focused melt flow and localized deformation in the upper mantle: Juxtaposition of replacive dunite and ductile shear zones in the Josephine peridotite, SW Oregon. *Journal of Geophysical Research: Solid Earth*, *100*(B1), pp.423-438.

K.R. Mehnert, W. Büsch, G. S., 1973. Initial melting at grain boundaries of quartz and feldspar in gneisses and granulites, Neues Jahrbuch f. *Mineralogie, Monatshefte,* 4, pp. 165-183.

Kruhl, J.H., 1996. Prism-and basal-plane parallel subgrain boundaries in quartz: A microstructural geothermobarometer. *Journal of metamorphic Geology*, *14*(5), pp.581-589.

Kuhlmann-Wilsdorf, D. and Hansen, N., 1991. Geometrically necessary, incidental and subgrain boundaries. *Scripta metallurgica et materialia*, *25*(7), pp.1557-1562.

Keller CB, Schoene B, Barboni M, Samperton KM, Husson JM (2015) Volcanic–plutonic parity and the differentiation of the continental crust. *Nature, 523*, pp.301–307.

Laporte, D., 1994. Wetting behavior of partial melts during crustal anatexis: the distribution of hydrous silicic melts in polycrystalline aggregates of quartz. *Contributions to Mineralogy and Petrology*, *116*(4), pp.486-499.

Law, R.D., 1990. Crystallographic fabrics: a selective review of their applications to research in structural geology. *Geological Society, London, Special Publications*, *54*(1), pp.335-352.

Law, R.D., 2014. Deformation thermometry based on quartz c-axis fabrics and recrystallization microstructures: A review. *Journal of Structural Geology*, *66*, pp.129-161.

Lee, A.L., Torvela, T., Lloyd, G.E. and Walker, A.M., 2018. Melt organisation and strain partitioning in the lower crust. *Journal of Structural Geology*, *113*, pp.188-199.

Lister, G.S. and Snoke, A.W., 1984. SC mylonites. *Journal of Structural Geology*, *6*(6), pp.617-638.

Lloyd, G.E., 2004. Microstructural evolution in a mylonitic quartz simple shear zone: the significant roles of dauphine twinning and misorientation. *Geological Society, London, Special Publications*, *224*(1), pp.39-61.

McNamara, D.D., Lister, A. and Prior, D.J., 2016. Calcite sealing in a fractured geothermal reservoir: Insights from combined EBSD and chemistry mapping. *Journal of Volcanology and Geothermal Research*, *323*, pp.38-52.

Menegon, L., Pennacchioni, G., Heilbronner, R. and Pittarello, L., 2008. Evolution of quartz microstructure and c-axis crystallographic preferred orientation within ductilely deformed granitoids (Arolla unit, Western Alps). *Journal of Structural Geology*, *30*(11), pp.1332-1347.

Menegon, L., Piazolo, S. and Pennacchioni, G., 2011. The effect of Dauphiné twinning on plastic strain in quartz. *Contributions to Mineralogy and Petrology*, *161*(4), pp.635-652.

Muller, N., Qi, R., Mackie, E., Pruess, K. and Blunt, M.J., 2009. CO2 injection impairment due to halite precipitation. *Energy procedia*, *1*(1), pp.3507-3514.

Ninham, B.W. and Parsegian, V.A., 1970. Van der Waals forces. *Biophysical journal*, *10*(7), pp.646-663.

Okudaira, T., Takeshita, T., Hara, I. and Ando, J.I., 1995. A new estimate of the conditions for transition from basal< a> to prism [c] slip in naturally deformed quartz. *Tectonophysics*, *250*(1-3), pp.31-46.

Okudaira, T. and Shigematsu, N., 2012. Estimates of stress and strain rate in mylonites based on the boundary between the fields of grain-size sensitive and insensitive creep. *Journal of Geophysical Research: Solid Earth*, *117*(B3).

Ostapenko, G.T., 1976. Excess pressure on the solid phases generated by hydration (according to experimental data on the hydration of periclase). *Traslated from Geokhimikiya*, *6*, pp.824-844.

Marchildon, N. and Brown, M., 2002. Grain-scale melt distribution in two contact aureole rocks: Implications for controls on melt localization and deformation. *Journal of Metamorphic Geology*, *20*(4), pp.381-396.

Menegon, L., Nasipuri, P., Stünitz, H., Behrens, H. and Ravna, E., 2011. Dry and strong quartz during deformation of the lower crust in the presence of melt. *Journal of Geophysical Research: Solid Earth*, *116*(B10).

Menegon, L., Fusseis, F., Stünitz, H. and Xiao, X., 2015. Creep cavitation bands control porosity and fluid flow in lower crustal shear zones. *Geology*, *43*(3), pp.227-230.

Parsons, A.J., Law, R.D., Lloyd, G.E., Phillips, R.J. and Searle, M.P., 2016. Thermo-kinematic evolution of the A nnapurna-D haulagiri H imalaya, central N epal: The C omposite O rogenic S ystem. *Geochemistry, Geophysics, Geosystems*, *17*(4), pp.1511-1539.

Passchier, C.W. and Simpson, C., 1986. Porphyroclast systems as kinematic indicators. *Journal of Structural Geology*, *8*(8), pp.831-843.

Passchier, C.W. and Trouw, R.A., 2005. *Microtectonics* (Vol. 1). Springer Science & Business Media.

Paterson, S.R., Vernon, R.H. and Tobisch, O.T., 1989. A review of criteria for the identification of magmatic and tectonic foliations in granitoids. *Journal of structural geology*, *11*(3), pp.349-363.

Paterson, M.S., 1995. A theory for granular flow accommodated by material transfer via an intergranular fluid. *Tectonophysics*, *245*(3-4), pp.135-151.

Paterson, M.S., 2001. A granular flow theory for the deformation of partially molten rock. *Tectonophysics*, *335*(1-2), pp.51-61.

Piazolo, S., Bestmann, M., Prior, D.J. and Spiers, C.J., 2006. Temperature dependent grain boundary migration in deformed-then-annealed material: observations from experimentally deformed synthetic rocksalt. *Tectonophysics*, *427*(1-4), pp.55-71.

Piazolo, S., Montagnat, M. and Blackford, J.R., 2008. Sub-structure characterization of experimentally and naturally deformed ice using cryo-EBSD. *Journal of Microscopy*, *230*(3), pp.509-519.

Piazolo, S., Montagnat, M. and Blackford, J.R., 2008. Sub-structure characterization of experimentally and naturally deformed ice using cryo-EBSD. *Journal of Microscopy*, *230*(3), pp.509-519.

Piazolo, S. and Jaconelli, P., 2014. Sillimanite deformation mechanisms within a Grt-Sil-Bt gneiss: effect of pre-deformation grain orientations and characteristics on mechanism, slip-system activation and rheology. *Geological Society, London, Special Publications*, *394*(1), pp.189-213.

Piazolo, S., Montagnat, M., Grennerat, F., Moulinec, H. and Wheeler, J., 2015. Effect of local stress heterogeneities on dislocation fields: Examples from transient creep in polycrystalline ice. *Acta Materialia*, *90*, pp.303-309.

Pitcher, W.S., 1979. The nature, ascent and emplacement of granitic magmas. *Journal of the Geological Society*, *136*(6), pp.627-662.

Prakash, A., Piazolo, S., Saha, L., Bhattacharya, A., Pal, D.K. and Sarkar, S., 2018. Deformation behavior of migmatites: insights from microstructural analysis of a garnet–sillimanite–mullite–quartz–feldspar-bearing anatectic migmatite at Rampura–Agucha, Aravalli–Delhi Fold Belt, NW India. *International Journal of Earth Sciences*, pp.1-28.

Prior, D.J., Boyle, A.P., Brenker, F., Cheadle, M.C., Day, A., Lopez, G., Peruzzo, L., Potts, G.J., Reddy, S., Spiess, R. and Timms, N.E., 1999. The application of electron backscatter diffraction and orientation contrast imaging in the SEM to textural problems in rocks. *American Mineralogist*, *84*(11-12), pp.1741-1759.

Prior, D.J., Wheeler, J., Peruzzo, L., Spiess, R. and Storey, C., 2002. Some garnet microstructures: an illustration of the potential of orientation maps and misorientation analysis in microstructural studies. *Journal of Structural Geology*, *24*(6-7), pp.999-1011.

Prior, D.J., Mariani, E. and Wheeler, J., 2009. EBSD in the earth sciences: applications, common practice, and challenges. In *Electron backscatter diffraction in materials science* (pp. 345-360). Springer, Boston, MA.

Poirier, J.P. and Nicolas, A., 1975. Deformation-induced recrystallization due to progressive misorientation of subgrains, with special reference to mantle peridotites. *The Journal of Geology*, *83*(6), pp.707-720.

Poirier, J.P. and Guillopé, M., 1979. Deformation induced recrystallization of minerals. *Bulletin de Mineralogie*, *102*(2), pp.67-74.

Putnis, A., 2002. Mineral replacement reactions: from macroscopic observations to microscopic mechanisms. *Mineralogical Magazine*, *66*(5), pp.689-708.

Putnis, A. and Austrheim, H., 2010. Fluid-induced processes: metasomatism and metamorphism. *Geofluids*, *10*(1-2), pp.254-269.

Ramsay, J.G., 1989. Emplacement kinematics of a granite diapir: the Chindamora batholith, Zimbabwe. *Journal of structural Geology*, *11*(1-2), pp.191-209.

Rapp, R.P., Watson, E.B. and Miller, C.F., 1991. Partial melting of amphibolite/eclogite and the origin of Archean trondhjemites and tonalites. *Precambrian Research*, *51*(1-4), pp.1-25.

Reddy, S.M., Timms, N.E., Pantleon, W. and Trimby, P., 2007. Quantitative characterization of plastic deformation of zircon and geological implications. *Contributions to Mineralogy and Petrology*, *153*(6), pp.625-645.

Rubie, D.C. and Gunter, W.D., 1983. The role of speciation in alkaline igneous fluids during fenite metasomatism. *Contributions to Mineralogy and Petrology*, *82*(2-3), pp.165-175.

Rubatto, D., Hermann, J. and Buick, I.S., 2006. Temperature and bulk composition control on the growth of monazite and zircon during low-pressure anatexis (Mount Stafford, central Australia). *Journal of Petrology*, *47*(10), pp.1973-1996.
.
Rosenberg, C.L. and Riller, U., 2000. Partial-melt topology in statically and dynamically recrystallized granite. *Geology*, *28*(1), pp.7-10.

Rosenberg, C.L., 2004. Shear zones and magma ascent: a model based on a review of the Tertiary magmatism in the Alps. *Tectonics*, *23*(3).

Rosenberg, C.L. and Handy, M.R., 2005. Experimental deformation of partially melted granite revisited: implications for the continental crust. *Journal of metamorphic Geology*, *23*(1), pp.19-28.

Rybacki, Erik, Richard Wirth, and Georg Dresen. "High-strain creep of feldspar rocks: Implications for cavitation and ductile failure in the lower crust." *Geophysical Research Letters* 35, no. 4 (2008).

Sawyer EW. Criteria for the recognition of partial melting. Physics and Chemistry of the Earth, Part A: Solid Earth and Geodesy. 1999 Jan 1; 24(3):269-79.

Sawyer, E.W., 2001. Melt segregation in the continental crust: distribution and movement of melt in anatectic rocks. *Journal of metamorphic Geology*, *19*(3), pp.291-309.

Sawyer, E.W., 2008. *Atlas of migmatites* (Vol. 9). NRC Research Press.

Scott, D.R. and Stevenson, D.J., 1986. Magma ascent by porous flow. *Journal of Geophysical Research: Solid Earth*, *91*(B9), pp.9283-9296.

Schulmann, K., Martelat, J.E., Ulrich, S., Lexa, O., Štípská, P. and Becker, J.K., 2008. Evolution of microstructure and melt topology in partially molten granitic mylonite: Implications for rheology of felsic middle crust. *Journal of Geophysical Research: Solid Earth*, *113*(B10).

Scherer, H.W. and Zhang, Y., 1999. Studies on the mechanisms of fixation and release of ammonium in paddy soils after flooding. I. Effect of iron oxides on ammonium fixation. *Journal of Plant Nutrition and Soil Science*, *162*(6), pp.593-597.

Scherer, G.W., 2004. Stress from crystallization of salt. *Cement and concrete research*, *34*(9), pp.1613-1624.

Spear, F.S. and Cheney, J.T., 1989. A petrogenetic grid for pelitic schists in the system SiO 2-Al 2 O 3-FeO-MgO-K 2 OH 2 O. *Contributions to Mineralogy and Petrology*, *101*(2), pp.149-164.

Spruzeniece, L. and Piazolo, S., 2015. Strain localization in brittle-ductile shear zones: fluid-abundant vs. fluid-limited conditions (an example from Wyangala area, Australia).

Spruzeniece, L., Piazolo, S. and Maynard-Casely, H.E., 2017. Deformation-resembling microstructure created by fluid-mediated dissolution–precipitation reactions. *Nature communications*, *8*, p.14032.

Smith, F.G., 1957. Decrepitation characteristics of igneous rocks. *The Canadian Mineralogist*, *6*(1), pp.78-86.

Stipp, M., Stünitz, H., Heilbronner, R. and Schmid, S.M., 2002. Dynamic recrystallization of quartz: correlation between natural and experimental conditions. *Geological Society, London, Special Publications*, *200*(1), pp.171-190.

Stipp, M., StuÈnitz, H., Heilbronner, R. and Schmid, S.M., 2002. The eastern Tonale fault zone: a 'natural laboratory'for crystal plastic deformation of quartz over a temperature range from 250 to 700 C. *Journal of Structural Geology*, *24*(12), pp.1861-1884.

Stipp, M. and Kunze, K., 2008. Dynamic recrystallization near the brittle-plastic transition in naturally and experimentally deformed quartz aggregates. *Tectonophysics*, *448*(1-4), pp.77-97.

Stuart, C.A., Piazolo, S. and Daczko, N.R., 2016. Mass transfer in the lower crust: Evidence for incipient melt assisted flow along grain boundaries in the deep arc granulites of Fiordland, New Zealand. *Geochemistry, Geophysics, Geosystems*, *17*(9), pp.3733-3753.

Stuart, C.A., Daczko, N.R. and Piazolo, S., 2017. Local partial melting of the lower crust triggered by hydration through melt–rock interaction: an example from Fiordland, New Zealand. *Journal of Metamorphic Geology*, *35*(2), pp.213-230.

Stuart CA, Piazolo S, Daczko NR. The recognition of former melt flux through high-strain zones. *J Metamorph Geol*. 2018;00: pp.1–21.

Taylor, S.R. and McLennan, S.M., 1995. The geochemical evolution of the continental crust. *Reviews of Geophysics*, *33*(2), pp.241-265.

Tommasi, A., Vauchez, A., Femandes, L.A. and Porcher, C.C., 1994. Magma-assisted strain localization in an orogen-parallel transcurrent shear zone of southern Brazil. *Tectonics*, *13*(2), pp.421-437.

Tubia, J.M. and Cuevas, J., 1986. High-temperature emplacement of the Los Reales peridotite nappe (Betic Cordillera, Spain). *Journal of Structural Geology*, *8*(3-4), pp.473-482.

Turcotte, D.L. and Ahern, J.L., 1978. A porous flow model for magma migration in the asthenosphere. *Journal of Geophysical Research: Solid Earth*, *83*(B2), pp.767-772.

Tullis, J.A., 1979. High temperature deformation of rocks and minerals. *Reviews of Geophysics*, *17*(6), pp.1137-1154.

Tullis, J., 1977. Preferred orientation of quartz produced by slip during plane strain. *Tectonophysics*, *39*(1-3), pp.87-102.

Tullis, J., 1970. Quartz: preferred orientation in rocks produced by Dauphiné twinning. *Science*, *168*(3937), pp.1342-1344.

Turner, F.J., 1981. *Metamorphic petrology: Mineralogical, field, and tectonic aspects*. McGraw-Hill Companies.

Turner, J.S. and Gustafson, L.B., 1981. Fluid motions and compositional gradients produced by crystallization or melting at vertical boundaries. *Journal of Volcanology and Geothermal Research*, *11*(2-4), pp.93-125.

Vance JA (1969) On synneusis. *Contrib Mineral Petrol, 24*, pp.7–29.

Vernooij, M.G., Kunze, K. and den Brok, B., 2006. 'Brittle'shear zones in experimentally deformed quartz single crystals. *Journal of Structural Geology*, *28*(7), pp.1292-1306.

Vernon, R.H., 2000. Review of microstructural evidence of magmatic and solid-state flow. *Visual Geosciences*, *5*(2), pp.1-23.

Vernon, R.H., Johnson, S.E. and Melis, E.A., 2004. Emplacement-related microstructures in the margin of a deformed pluton: the San José tonalite, Baja California, México. *Journal of Structural Geology*, *26*(10), pp.1867-1884.

Vernon, R.H. and Paterson, S.R., 2008. How late are K-feldspar megacrysts in granites?. *Lithos*, *104*(1-4), pp.327-336.

Vernon, R.H., 2011. Microstructures of melt-bearing regional metamorphic rocks. *Geological Society of America Memoirs*, *207*, pp.1-11.

Vukmanovic, Z., Holness, M.B., Monks, K. and Andersen, J.C.Ø., 2018. The Skaergaard trough layering: sedimentation in a convecting magma chamber. *Contributions to Mineralogy and Petrology*, *173*, pp.1-18.

Wang, W., Dunkley, E., Clarke, G.L. and Daczko, N.R., 2014. The evolution of zircon during low-P partial melting of metapelitic rocks: theoretical predictions and a case study from Mt Stafford, central Australia. *Journal of Metamorphic Geology*, *32*(8), pp.791-808.

Watt, G.R., Oliver, N.H.S. and Griffin, B.J., 2000. Evidence for reaction-induced microfracturing in granulite facies migmatites. *Geology*, *28*(4), pp.327-330.

Weinberg, R.F., Mark, G. and Reichardt, H., 2009. Magma ponding in the Karakoram shear zone, Ladakh, NW India. *Geological Society of America Bulletin*, *121*(1-2), pp.278-285.

Weinberg, R.F. and Regenauer-Lieb, K., 2010. Ductile fractures and magma migration from source. *Geology*, *38*(4), pp.363-366.

Weinberg, R.F., Veveakis, E. and Regenauer-Lieb, K., 2015. Compaction-driven melt segregation in migmatites. *Geology*, *43*(6), pp.471-474.

Wellman, H.W. and Wilson, A.T., 1965. Salt weathering, a neglected geological erosive agent in coastal and arid environments. *Nature*, *205*(4976), p.1097.

Wheeler, J., Prior, D., Jiang, Z., Spiess, R. and Trimby, P., 2001. The petrological significance of misorientations between grains. *Contributions to mineralogy and petrology*, *141*(1), pp.109-124.

Wheeler, J., Mariani, E., Piazolo, S., Prior, D.J., Trimby, P. and Drury, M.R., 2009. The weighted Burgers vector: a new quantity for constraining dislocation densities and types using electron backscatter diffraction on 2D sections through crystalline materials. *Journal of microscopy*, *233*(3), pp.482-494.

White, R.W., Powell, R. and Halpin, J.A., 2004. Spatially-focussed melt formation in aluminous metapelites from Broken Hill, Australia. *Journal of Metamorphic Geology*, *22*(9), pp.825-845.

Whitney, D.L. and Evans, B.W., 2010. Abbreviations for names of rock-forming minerals. *American mineralogist*, *95*(1), pp.185-187.Wintsch, R.P. and Yeh, M.W., 2013. Oscillating brittle and viscous behavior through the earthquake cycle in the Red River Shear Zone: Monitoring flips between reaction and textural softening and hardening. *Tectonophysics*, *587*, pp.46-62.

Wolf, M.B. and Wyllie, P.J., 1994. Dehydration-melting of amphibolite at 10 kbar: the effects of temperature and time. *Contributions to Mineralogy and Petrology*, *115*(4), pp.369-383.

Závada, P., Schulmann, K., Konopásek, J., Ulrich, S. and Lexa, O., 2007. Extreme ductility of feldspar aggregates—Melt-enhanced grain boundary sliding and creep failure: Rheological implications for felsic lower crust. *Journal of Geophysical Research: Solid Earth*, *112*(B10).

Závada, P., Schulmann, K., Racek, M., Hasalová, P., Jeřábek, P., Weinberg, R.F., Štípská, P. and Roberts, A., 2018. Role of strain localization and melt flow on exhumation of deeply subducted continental crust. *Lithosphere*, *10*(2), pp.217-238.

.